LETTER

https://doi.org/10.1038/s41586-018-0746-2

Chemical differentiation, cold storage and remobilization of magma in the Earth's crust

M. D. Jackson[1]*, J. Blundy[2] & R. S. J. Sparks[2]

The formation, storage and chemical differentiation of magma in the Earth's crust is of fundamental importance in igneous geology and volcanology. Recent data are challenging the high-melt-fraction 'magma chamber' paradigm that has underpinned models of crustal magmatism for over a century, suggesting instead that magma is normally stored in low-melt-fraction 'mush reservoirs'[1–9]. A mush reservoir comprises a porous and permeable framework of closely packed crystals with melt present in the pore space[1,10]. However, many common features of crustal magmatism have not yet been explained by either the 'chamber' or 'mush reservoir' concepts[1,11]. Here we show that reactive melt flow is a critical, but hitherto neglected, process in crustal mush reservoirs, caused by buoyant melt percolating upwards through, and reacting with, the crystals[10]. Reactive melt flow in mush reservoirs produces the low-crystallinity, chemically differentiated (silicic) magmas that ascend to form shallower intrusions or erupt to the surface[11–13]. These magmas can host much older crystals, stored at low and even sub-solidus temperatures, consistent with crystal chemistry data[6–9]. Changes in local bulk composition caused by reactive melt flow, rather than large increases in temperature, produce the rapid increase in melt fraction that remobilizes these cool- or cold-stored crystals. Reactive flow can also produce bimodality in magma compositions sourced from mid- to lower-crustal reservoirs[14,15]. Trace-element profiles generated by reactive flow are similar to those observed in a well studied reservoir now exposed at the surface[16]. We propose that magma storage and differentiation primarily occurs by reactive melt flow in long-lived mush reservoirs, rather than by the commonly invoked process of fractional crystallization in magma chambers[14].

Magma reservoirs occur at several depths within the crust and typically grow incrementally through the intrusion of dykes or sills[1,11,13,16,17]. High melt fractions must sometimes be present in these reservoirs to produce eruptible, low-crystallinity magmas[1,7–9,13]. However, geophysical data suggest that reservoirs have low melt fraction even beneath active volcanoes[2–5] and crystal chemistry data indicate that long-term magma storage occurs at low or even sub-solidus temperatures[6–9]. High melt fractions are therefore ephemeral; yet geochemical models typically assume that differentiation occurs by crystal fractionation from low-crystallinity magmas[11,14]. Moreover, geochronological data demonstrate that crustal magma reservoirs can be long-lived, spanning hundreds of thousands to millions of years[17–21]. Existing models of crustal magma storage and differentiation cannot reconcile these conflicting observations.

We use numerical modelling to investigate the storage and chemical differentiation of magma in crustal reservoirs. The model describes repeated intrusion of mafic to intermediate sills into the mid- to lower crust[12,13,16,21–23], the associated transport of heat via conduction and advection and, in a key advance, mass transport via reactive flow of buoyant melt through the compacting crystal framework[10]. Transport of chemical components by the melt modifies the local bulk composition, and melt fraction changes in response to the chemical reactions that maintain local thermodynamic equilibrium. Phase behaviour is modelled using a two-component, eutectic phase diagram that, although greatly simplified compared to natural systems, captures the critically important impact of bulk composition on melting behaviour and the complex nonlinear relationships between composition, melt fraction and permeability (see Methods)[10]. Melting relationships obtained from the phase diagram approximate common crustal igneous systems (Extended Data Fig. 1). The concentration of an incompatible trace element is also modelled assuming a constant partition coefficient.

Typical results are shown in Fig. 1 (see also Supplementary Video 1). In this example, 100-m-thick basalt (mafic) sills are intruded randomly over a depth range of 600 m, initially at 18 km depth and then around a depth that is controlled by the density contrast between intruding magma and host mush, reflecting the evolving reservoir composition and melt fraction (see Methods). We emplace 7.8 km of basalt in total, at an average rate of 5 mm yr^{-1} that is typical of crustal magmatic systems[22–24], into solid crust with an initial geotherm[21–23] of 20 K km^{-1}. Our example was chosen to facilitate comparison with data from a well studied deep crustal section[16,21]. The key findings are replicated over the depth range of 10–30 km typical of many crustal magma reservoirs and following intrusion of intermediate as well as mafic magma, using model parameters over a wide range that is reasonable for such systems (see Methods and Extended Data Table 1).

Initially, following each sill intrusion, the melt fraction rapidly falls to zero so there is no persistent magma reservoir (Supplementary Video 1 and Extended Data Fig. 2). This is the 'incubation phase' of the incipient magma reservoir, observed also in models that neglect reactive flow[22,23]. However, in our model, chemical differentiation occurs within each intrusion before it solidifies, with more evolved melt (enriched in the incompatible trace element) accumulating at the top of the intrusion, and more refractory and depleted crystals accumulating at the base. The rapid increase in crystallinity traps the magma at the site of intrusion, but differentiation creates compositional contrasts that cause the intrusion depth to increase progressively (Supplementary Video 1 and Extended Data Fig. 3a).

The incubation phase ends when the melt fraction is greater than zero between successive sill intrusions, whereupon a magma reservoir has formed (Fig. 1a; Supplementary Video 1). Melt is now persistently present, but melt fraction remains low except for a brief period after each new intrusion (Extended Data Fig. 2b). The reservoir comprises a mush, rather than a high-melt-fraction magma chamber. Reactive flow now considerably modifies the predicted reservoir behaviour compared to previous models[22,23].

Buoyant melt migrates upwards through the mush, accumulating in the upper part of the reservoir because it cannot travel beyond the solidus isotherm where the melt fraction and permeability fall to zero (Supplementary Video 1). Melt composition evolves as it flows into, and reacts with, progressively cooler mush. Reactive flow reduces, or removes, early-formed compositional contrasts, such that the locally varying melt fraction controls the depth of later sill intrusions, which decreases as melt migrates upwards (see Methods). This is the 'growing phase' of the reservoir.

The growing phase ends when melt accumulates below the solidus isotherm to form a high-melt-fraction (typically >0.7) layer

[1]Department of Earth Science and Engineering, Imperial College London, London, UK. [2]School of Earth Sciences, University of Bristol, Bristol, UK. *e-mail: m.d.jackson@imperial.ac.uk

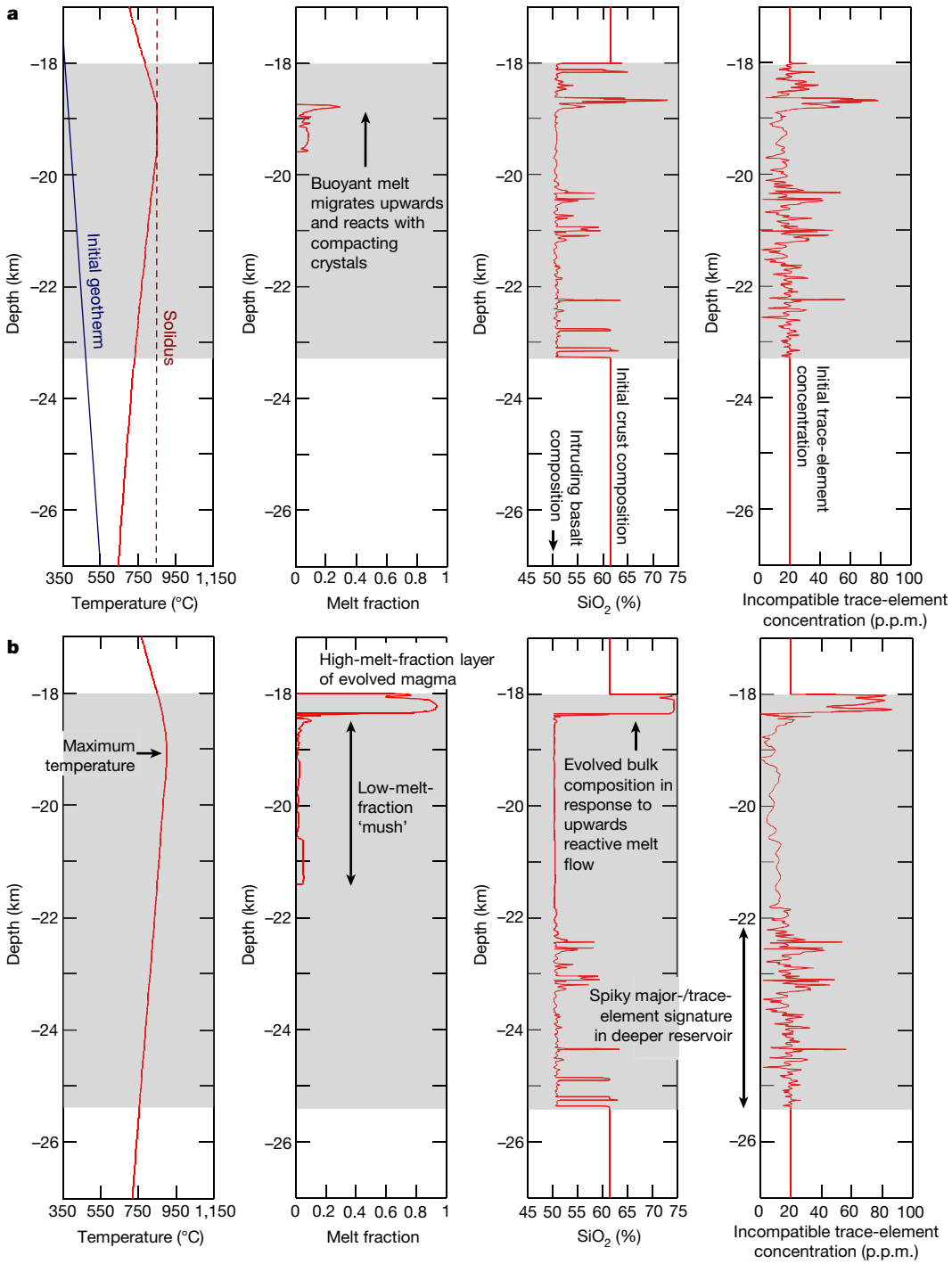

Fig. 1 | Temperature, melt fraction, bulk composition and incompatible trace-element concentration as a function of depth during the growing and active phases of the reservoir. a, **b**, Snapshots at 0.97 Myr (**a**) and 1.39 Myr (**b**) following the onset of sill intrusions, taken from Supplementary Video 1. At early times (not shown; see Extended Data Fig. 3a), during the incubation phase, individual sills cool rapidly. At later times (**a**), during the growing phase, a persistent mush reservoir forms but the melt fraction is low. Buoyant melt migrates upwards and begins to accumulate at the top of the mush. During the active phase (**b**), the accumulating melt forms a high-melt-fraction layer containing mobile magma. The composition of the melt in the layer is evolved and enriched in incompatible trace elements. Elsewhere in the mush, the melt fraction remains low. At late times (not shown; see Extended Data Fig. 3b) during the waning phase, sill intrusions cease and the mush cools and solidifies. To illustrate the key processes, intruding basalt and crust are assumed in this example to have the same initial incompatible trace-element concentration. Shaded areas in all plots denote the vertical extent of basalt intrusions at that time. Equivalent results for sill intrusions at 10 km depth are shown in Extended Data Fig. 5.

overlying a thick (several kilometres), low-melt-fraction (typically <0.2) mush (Fig. 1b and Supplementary Video 1). The melt-rich layer contains chemically differentiated felsic magma and can grow to several hundreds of metres in thickness. Although not captured by the model, buoyant magma in the layer will be prone to leave the reservoir to produce shallower intrusions or volcanic eruptions[25,26]. Once magma leaves, a new layer grows by the same mechanism (see Methods).

This is the 'active phase', during which the reservoir can deliver evolved, low-crystallinity magma (Extended Data Fig. 2b). We suggest that, although geophysical surveys are probing active reservoirs, they image only the low-melt-fraction mush[2–5]; the overlying

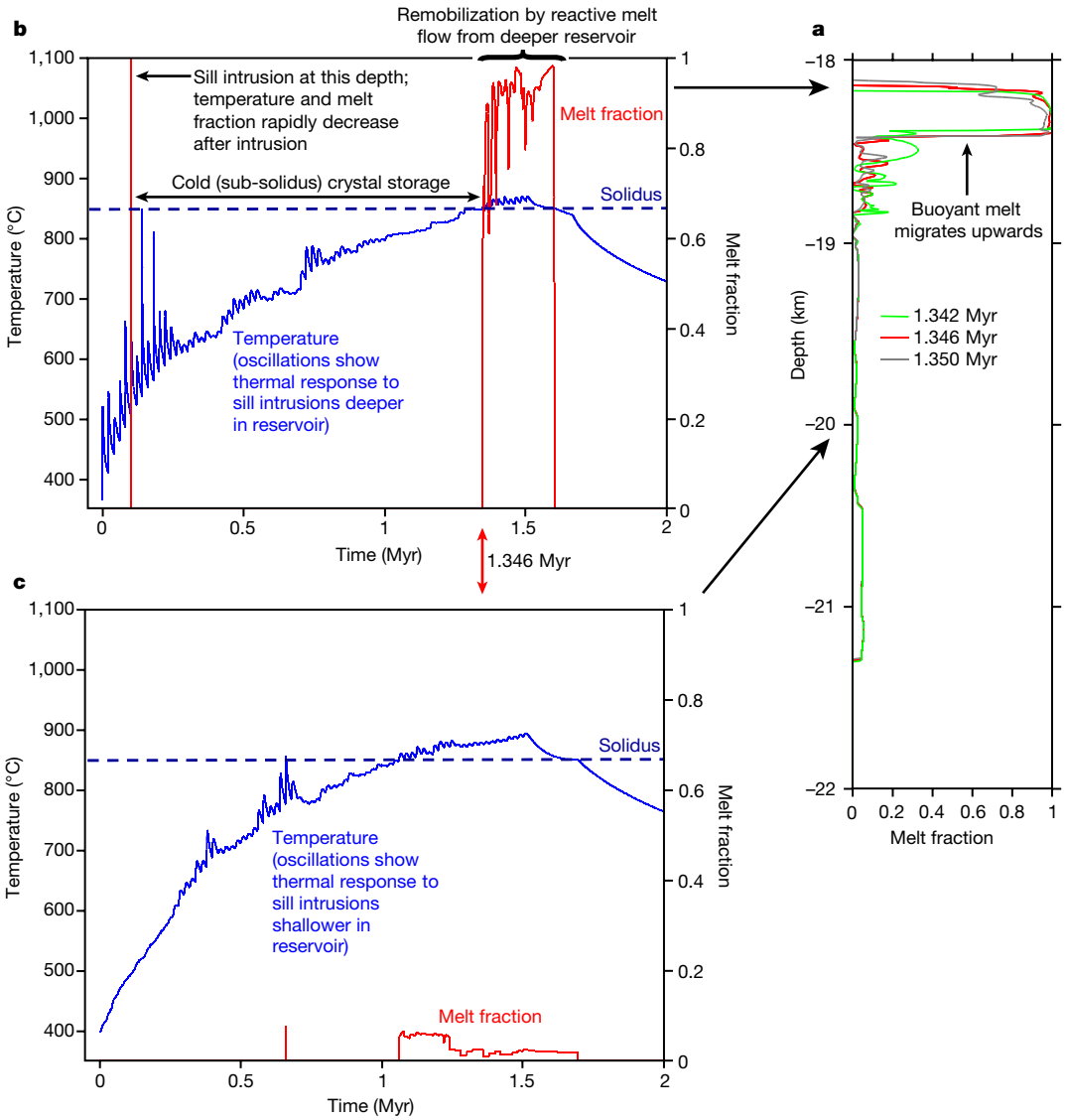

Fig. 2 | Cold storage and rapid remobilization of magma. a, Melt fraction as a function of depth at three different snapshots in time: at 1.346 Myr following the onset of sill intrusions and at 4 thousand years (kyr) before and 4 kyr after that time. Reactive flow of buoyant melt produces a high-melt-fraction layer that migrates upwards. **b**, Temperature and melt fraction as a function of time at a depth of 18.2 km, close to the top of the reservoir. Similar results are obtained over the depth range 18–18.5 km. Early sill intrusions rapidly cool and crystallize. The crystals are kept in 'cold storage' at sub-solidus temperature, but the temperature gradually increases in response to sill intrusions deeper in the reservoir. Soon (<0.3 kyr) after the temperature exceeds the solidus, the high-melt-fraction layer arrives at this depth (the red arrow denotes the corresponding snapshot in **a**) and the reservoir is remobilized: the melt fraction increases rapidly to form a low-crystallinity magma. The melt fraction increases much more rapidly and to a higher value than would be possible by melting alone. **c**, Temperature and melt fraction as a function of time at a depth of 20 km. Similar results are obtained over the depth range 18.5–21.5 km. The melt fraction remains low because reactive flow has left a refractory residue at this depth. There is no remobilization, despite the increase in temperature. Data extracted from Supplementary Video 1. Equivalent results for intrusions at 10 km depth are shown in Extended Data Fig. 6.

high-melt-fraction layers are not observed, because they are ephemeral or too thin to be resolved. Geophysical detection of such a layer would suggest that magma mobilization (and possible eruption) was imminent[7].

When intrusion of new sills ends, reactive flow continues wherever the temperature is above the solidus but, overall, the reservoir cools. This is the 'waning phase' (Supplementary Video 1; Extended Data Fig. 3b) that persists until the mush has completely solidified (Extended Data Fig. 2b). If exhumed, the resulting body of rock is termed a deep crustal section, of which there are several natural examples[16,21].

During the active phase, the high-melt-fraction layer forms towards the top of the reservoir where the temperature is low, rather than at the highest temperature (Fig. 1b). This counter-intuitive result is a consequence of reactive flow, whereby melt accumulation causes the local bulk composition to evolve towards the eutectic. Melt composition in more chemically complex systems will evolve towards other low-variance states such as cotectics, peritectics or multiple-saturation points (see Methods), but the overall behaviour will be similar. A key finding here is that high-melt-fraction layers in crustal mush reservoirs can form in response to changes in bulk composition caused by reactive melt flow, rather than by large increases in temperature.

Magma in a high-melt-fraction layer contains about 10% crystals (Fig. 2a). These 'antecrysts' can long pre-date magma formation, because they derive from crystallization of early sills at the top of the reservoir. Once formed, the antecrysts are stored at near- or sub-solidus temperature (that is, 'cool' or 'cold'; Fig. 2b). The local temperature gradually increases in response to ongoing intrusion of sills deeper in the reservoir and, eventually, exceeds the solidus. Soon afterwards, buoyant, evolved melt, migrating upwards through the pore space, accumulates around these older antecrysts, causing the local melt

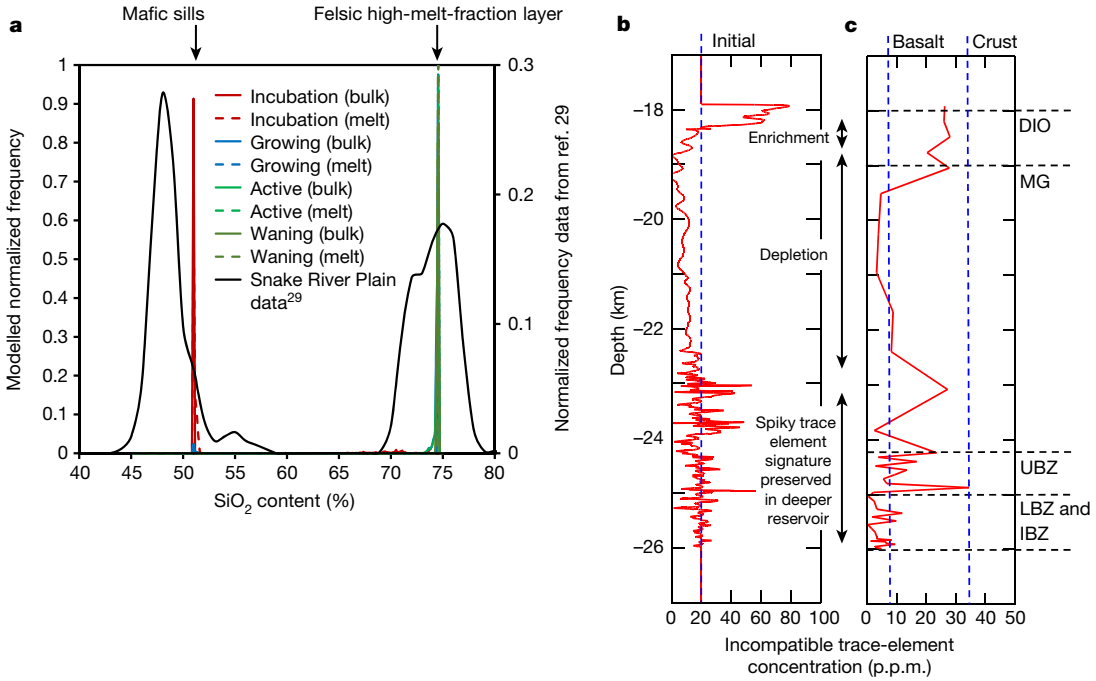

Fig. 3 | Geochemical consequences of reactive melt flow in crustal magma reservoirs. a, SiO_2 content of low-crystallinity (crystal fraction <30%) magmas. Solid curves show bulk magma composition (melt plus crystals); dashed curves show melt composition alone. The peak at low SiO_2 corresponds to magma within the intruding sills; the peak at high SiO_2 corresponds to magma within high-melt-fraction layers near the top of the reservoir. Also shown for comparison are data from the Snake River Plain[29]. The bimodality is clear, although the basalt has a lower SiO_2 content than modelled here. Results for different intruding sill compositions are shown in Extended Data Fig. 7. **b**, **c**, Modelled and observed neodymium concentration along a palaeo-vertical transect through the Upper Mafic Complex in the Ivrea-Verbano zone. LBZ, Lower Basal Zone; IBZ, Intermediate Basal Zone; UBZ, Upper Basal Zone; MG, main gabbro; and DIO, diorite[16]. Both modelled (**b**) and observed[16] (**c**) data show a spiky profile at the base of the reservoir, depletion in the middle part of the reservoir and enrichment at the top.

fraction to increase rapidly and by far more than would be possible by heating alone (Fig. 2b)[6,7,18,27]. Cold mush is remobilized here not by a substantial increase in temperature, but by buoyancy-driven reactive flow supplying evolved melt from deeper, more refractory parts of the reservoir, where temperature can be high but the melt fraction remain low (Fig. 2c). Remobilization is primarily caused by changes in local bulk composition, rather than temperature.

In our example, melt accumulation forms a low-crystallinity magma a few centuries after the local temperature exceeds the solidus, yet the magma contains antecrysts formed up to about 1–1.4 millions of years (Myr) earlier (Fig. 2b). The range of antecryst ages reflects the timing of sill intrusions relative to the timing of melt accumulation. Crystal chemistry data show cool or cold storage and remobilization of older antecrysts hosted by younger felsic magma[6–9]; our results suggest that this could result from reactive melt flow accumulating young, felsic melt within older mush. The antecrysts are not in equilibrium with the younger melt, creating disequilibrium crystal textures such as partial resorption. Flow of buoyant melt into the high-melt-fraction layer

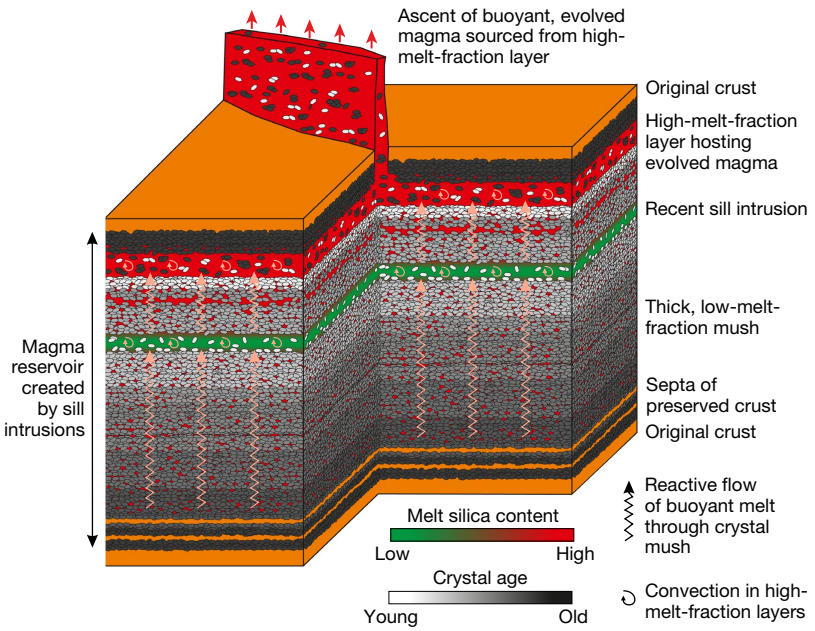

Fig. 4 | Reactive flow of buoyant melt at low melt fraction. Reactive flow is a critical mechanism controlling magma storage, accumulation and differentiation in mid- to lower-crustal reservoirs. The middle and lower parts of the reservoir comprise a thick (several kilometres) mush layer, with low and relatively uniform melt fraction, formed by early sill intrusions during the incubation and growing phases. This layer is typically imaged in geophysical data. During the active phase, the upper part of the reservoir comprises transient layers containing either intermediate/mafic or felsic magma, which can feed shallower intrusions or surface eruptions. The felsic magma layer is formed in response to changes in local bulk composition caused by upward reactive flow of buoyant melt through the mush. The evolved melt accumulates around older antecrysts, which may have formed during the earliest sill intrusions and hence long pre-date magma formation. In the schematic shown here, the felsic magma hosts a mixture of old and young antecrysts. The old antecrysts were formed during early sill intrusions; the young antecrysts formed during late sill intrusions at similar depth.

will drive convective overturn and homogenization before, or during, evacuation of magma, yielding a range of antecryst ages that may span the entire reservoir history[28].

Magmas in the high-melt-fraction layers have evolved composition. Conversely, magmas in the sills shortly after intrusion have compositions close to that of the intruded basalt. Low-crystallinity, mafic or felsic magmas can therefore leave the reservoir, but not magmas with intermediate composition. Many volcanic settings are characterized by bimodal volcanism (the 'Daly Gap'), especially in oceanic settings (hotspots and island arc environments) and continental hotspots (Fig. 3a)[14,15,29]. Our results suggest that compositional bimodality is another consequence of differentiation by reactive melt flow in mush reservoirs. However, not all systems show bimodality[30]. Intermediate compositions could result from magma mixing[15] or differentiation within multiple mush reservoirs comprising a vertically extensive magmatic system[1].

The modelled incompatible trace-element concentration in the solidified reservoir shows a characteristic pattern. Towards the base, the spiky signature produced by differentiation in each sill during the incubation phase is preserved (Fig. 3b). In the upper part, the profile is smoother and shows depletion relative to the initial concentration, reflecting extraction of melt. The top shows enrichment, reflecting accumulation of melt during the growing and active phases. Data from a deep crustal section show a similar pattern (Fig. 3c)[16]. We suggest that this pattern is another characteristic product of reactive melt flow in crustal mush reservoirs. Reactive melt flow at low melt fraction, rather than fractional crystallization at high melt fraction, is the dominant mechanism controlling magma storage, accumulation and chemical differentiation in the continental crust (Fig. 4).

Online content

Any methods, additional references, Nature Research reporting summaries, source data, statements of data availability and associated accession codes are available at https://doi.org/10.1038/s41586-018-0746-2.

Received: 19 December 2017; Accepted: 2 October 2018;
Published online 3 December 2018.

1. Cashman, K. V., Sparks, R. S. J. & Blundy, J. D. Vertically extensive and unstable magmatic systems: a unified view of igneous processes. *Science* https://doi.org/10.1126/science.aag3055 (2017).
2. Huang, H. H. et al. The Yellowstone magmatic system from the mantle plume to the upper crust. *Science* https://doi.org/10.1126/science.aaa5648 (2015).
3. Paulatto, M. et al. Magma chamber properties from integrated seismic tomography and thermal modeling at Montserrat. *Geochem. Geophys. Geosyst.* **13**, (2012).
4. Hill, G. J. et al. Distribution of melt beneath Mount St. Helens and Mount Adams inferred from magnetotelluric data. *Nat. Geosci.* **2**, 785–789 (2009).
5. Ward, K. M., Zandt, G., Beck, S. L., Christensen, D. H. & McFarlin, H. Seismic imaging of the magmatic underpinnings beneath the Altiplano-Puna volcanic complex from the joint inversion of surface wave dispersion and receiver functions. *Earth Planet. Sci. Lett.* **404**, 43–53 (2014).
6. Rubin, A. E. et al. Rapid cooling and cold storage in a silicic magma reservoir recorded in individual crystals. *Science* https://doi.org/10.1126/science.aam8720 (2017).
7. Cooper, K. M. & Kent, A. J. R. Rapid remobilization of magmatic crystals kept in cold storage. *Nature* **506**, 480–483 (2014).
8. Szymanowski, D. et al. Protracted near-solidus storage and pre-eruptive rejuvenation of large magma reservoirs. *Nat. Geosci.* **10**, 777–782 (2017).
9. Andersen, N. L., Jicha, B. R., Singer, B. S. & Hildreth, W. Incremental heating of Bishop Tuff sanidine reveals preeruptive radiogenic Ar and rapid remobilization from cold storage. *Proc. Natl Acad. Sci. USA* **114**, 12407–12412 (2017).
10. Solano, J. M. S., Jackson, M. D., Sparks, R. S. J. & Blundy, J. D. Evolution of major and trace element composition during melt migration through crystalline mush: implications for chemical differentiation in the crust. *Am. J. Sci.* **314**, 895–939 (2014).
11. Glazner, A. F., Bartley, J. M., Coleman, D. S., Gray, W. & Taylor, R. Z. Are plutons assembled over millions of years by amalgamation from small magma chambers? *GSA Today* **14**, 4–12 (2004).
12. Sisson, T. W., Ratajeski, K., Hankins, W. B. & Glazner, A. F. Voluminous granitic magmas from common basaltic sources. *Contrib. Mineral. Petrol.* **148**, 635–661 (2005).
13. Rudnick, R. L. Making continental crust. *Nature* **378**, 571–578 (1995).
14. Keller, B. C., Schoene, B., Barbonu, M., Samperton, K. M. & Husson, J. M. Volcanic–plutonic parity and the differentiation of the continental crust. *Nature* **523**, 301–307 (2015).
15. Reubi, O. & Blundy, J. A dearth of intermediate melts at subduction zone volcanoes and the petrogenesis of arc andesites. *Nature* **461**, 1269–1273 (2009).
16. Voshage, H. et al. Isotopic evidence from the Ivrea Zone for a hybrid lower crust formed by magmatic underplating. *Nature* **347**, 731–736 (1990).
17. Coleman, D. S., Gray, W. & Glazner, A. F. Rethinking the emplacement and evolution of zoned plutons: geochronologic evidence for incremental assembly of the Tuolumne Intrusive Suite. *Calif. Geol.* **32**, 433–436 (2004).
18. Barboni, M. et al. Warm storage for arc magmas. *Proc. Natl Acad. Sci. USA* **113**, 13959–13964 (2016).
19. Deering, C. D. et al. Zircon record of the plutonic-volcanic connection and protracted rhyolite melt evolution. *Geology* **44**, 267–270 (2016).
20. Frazer, R. E., Coleman, D. S. & Mills, R. D. Zircon U-Pb geochronology of the Mount Givens granodiorite: implications for the genesis of large volumes of eruptible magma. *J. Geophys. Res. Solid Earth* **119**, 2907–2924 (2014).
21. Peressini, G., Quick, J. E., Sinigoi, S., Hofmann, A. W. & Fanning, M. Duration of a large mafic intrusion and heat transfer in the lower crust: a SHRIMP U-Pb zircon study in the Ivrea-Verbano zone (Western Alps, Italy). *J. Petrol.* **48**, 1185–1218 (2007).
22. Annen, C., Blundy, J. D. & Sparks, R. S. J. The genesis of intermediate and silicic magmas in deep crustal hot zones. *J. Petrol.* **47**, 505–539 (2006).
23. Karakas, O., Degruyter, W., Bachmann, O. & Dufek, J. Lifetime and size of shallow magma bodies controlled by crustal-scale magmatism. *Nat. Geosci.* **10**, 446–450 (2017).
24. Crisp, J. A. Rates of magma emplacement and volcanic output. *J. Volcanol. Geotherm. Res.* **20**, 177–211 (1984).
25. Malfait, W. J. et al. Supervolcano eruptions driven by melt buoyancy in large silicic magma chambers. *Nat. Geosci.* **7**, 122–125 (2014).
26. Keller, T., May, D. A. & Kaus, B. J. P. Numerical modelling of magma dynamics coupled to tectonic deformation of lithosphere and crust. *Geophys. J. Int.* **195**, 1406–1442 (2013).
27. Huber, C., Bachmann, O. & Dufek, J. The limitations of melting on the reactivation of silicic mushes. *J. Volcanol. Geotherm. Res.* **195**, 97–105 (2010).
28. Bergantz, G. W., Schleicher, J. M. & Burgisser, A. Open-system dynamics and mixing in magma mushes. *Nat. Geosci.* **8**, 793–796 (2015).
29. Ellis, B. S. et al. Rhyolitic volcanism of the central Snake River Plain: a review. *Bull. Volcanol.* **75**, 745 (2013).
30. Bachmann, O. & Huber, C. Silicic magma reservoirs in the Earth's crust. *Am. Mineral.* **101**, 2377–2404 (2016).

Acknowledgements M.D.J. and J.B. acknowledge funding from NERC Grant NE/P017452/1 "From arc magmas to ores (FAMOS): A mineral systems approach". This paper is FAMOS contribution F05. M.D.J. also acknowledges sabbatical support from the Department of Earth Science and Engineering, Imperial College London, during which part of the research reported here was undertaken. R.S.J.S. acknowledges support from a Leverhulme Trust Emeritus Fellowship.

Reviewer information *Nature* thanks O. Bachmann, C. Till and the other anonymous reviewer(s) for their contribution to the peer review of this work.

Author contributions M.D.J. wrote the code and produced the numerical results. J.B. prepared the phase equilibria model and calibrated this to experimental data. R.S.J.S. provided information on context and background for the study. All authors jointly designed the numerical experiments presented and drafted the manuscript text. M.D.J. prepared the figures.

Competing interests The authors declare no competing interests.

Additional information
Extended data is available for this paper at https://doi.org/10.1038/s41586-018-0746-2.
Supplementary information is available for this paper at https://doi.org/10.1038/s41586-018-0746-2.
Reprints and permissions information is available at http://www.nature.com/reprints.
Correspondence and requests for materials should be addressed to M.D.J.
Publisher's note: Springer Nature remains neutral with regard to jurisdictional claims in published maps and institutional affiliations.

METHODS

Model formulation. To understand processes within crustal mush reservoirs, a quantitative model is required that includes three key features. First, the model must include the addition of hot magma or heat to initially solid crust, in order to create and grow the reservoir[22,23,31–34]. Second, the model must include the relative motion of melt and crystals, to allow chemical differentiation[10,34–37]. Third, the model must operate primarily at low melt fraction, consistent with a wealth of evidence that crustal magma reservoirs are normally low-melt-fraction mushes rather than high-melt-fraction magma chambers[1–9,38,39]. At low melt fraction, a magma reservoir comprises a mush of crystals forming a solid framework with melt distributed along grain boundaries[1,10,39–41]. At higher melt fraction, the reservoir comprises a slurry of melt containing suspended crystals that can flow via fractures, faults or other pathways to be intruded at shallower depths or erupt at the surface[1,26,39,40]. The latter process is not modelled explicitly in this study.

The intrusion of magma to form sills can occur in numerous tectonic settings, providing both a source of heat and a source of magma that can differentiate to produce evolved melt[1,13,16,17,21–23,31–33]. Here we follow earlier numerical approaches and model the repetitive intrusion of sills into the mid- to lower crust (modelling magma reservoirs at depths over the range 10–30 km), consistent with numerous contemporary magma reservoirs imaged in geophysical data and magma reservoirs interpreted to exist in deep crustal sections[2–5,16,21–23,31–34,42–44]. It is assumed that the magma in the sills is delivered from some deeper reservoir in the crust or upper mantle. In most of the example cases shown, the intruding magma is mantle-derived basalt, recognizing that crustal magmatism is largely driven by basalt[13] and consistent with numerous natural examples[16,21,23,42–44]. However, in a later section we also show results for a case when the intruding sills contain more evolved (intermediate) magma.

Most models of repetitive sill intrusion do not include relative motion of melt and crystals and, therefore, there is no chemical differentiation: the bulk composition of the mush reservoir remains constant[22,23,31–33]. Here, it is assumed that melt within the mush reservoir, produced by cooling and crystallization of the intruded sills and also heating and melting of the surrounding crust, is present along grain boundaries and forms an interconnected network at low melt fraction[10,39–41]. The melt is buoyant because it is less dense than the surrounding crystals, so a pressure gradient is present that causes upward flow of melt relative to the crystalline matrix[10,34,39]. The matrix can deform in response to melt flow[45–47]. This coupled process of melt migration and matrix deformation is termed compaction[48]. There is abundant evidence that compaction occurs in a wide variety of crustal igneous systems, and our assumptions are consistent with previous models of compaction[10,26,34,48–52].

Melt flow along grain boundaries in a mush reservoir allows efficient exchange of heat and mass between melt and solid phases, so that in most of the mush and over most of its lifetime, the phases remain in local thermal and chemical equilibrium[53]. The local bulk composition of the mush therefore changes as the melt migrates upwards and the crystals compact downwards. To capture this, our model includes component transport and chemical reaction[10,36,37,54]. The results shown here demonstrate that reactive flow of melt is a critically important process controlling the storage, accumulation and chemical evolution of magma within the mush reservoir.

Governing equations and method of solution. The governing equations and method of solution are modified from Solano et al.[10]. The enthalpy method is used to describe conservation of heat[55] and a binary eutectic phase diagram is used to describe solid and melt compositions, assuming local thermodynamic equilibrium[10,37].

In common with many previous studies, compaction is modelled using a modified version of the McKenzie formulation[48], assuming that deformation of the matrix occurs by melt-enhanced diffusion creep[45–47]. This is reasonable in supra-solidus mush reservoirs deforming at low strain rates ($\ll 10^{-15}$ s^{-1}) and yields a Newtonian rheology for the mush[56]. The matrix shear viscosity is assumed to be constant, but the matrix bulk viscosity has a power-law relationship with melt fraction[26,50,57]. The melt is also assumed to have a Newtonian rheology, which is reasonable for crystal-free melts containing a few weight per cent water[57,58].

Surface tension and interphase pressure are neglected. The compaction formulation is currently being extended to include these potentially important effects, but a single, self-consistent model that includes phase change has not yet been presented[59–63]. Differential stresses (imposed by tectonic forces) and magma chamber over-pressuring and loading[64] are also neglected, recognizing that at least some grain-boundary flow is essential to separate melt and crystals in a mush reservoir and buoyancy is always available to drive this. Volatiles are assumed to remain in solution, so are not present as a separate phase. In shallow crustal reservoirs, an exsolved volatile phase probably plays an important part in controlling phase relations and melt flow, and in driving magma mobilization[65,66].

As outlined in Solano et al.[10], the transport of heat, mass and components is modelled in one dimension, using a continuum formulation of the governing conservation equations. Typical sill intrusions and crustal mush reservoirs have high aspect ratio[2–5,16,21,38,42–44,67,68]. Given this, and the predominantly vertical flow of buoyant melt in the mush, a one-dimensional model is a reasonable starting point to determine the effects of reactive melt flow on magma storage and differentiation. However, a one-dimensional model does not admit the formation of high-porosity, sub-vertical channels caused by reactive infiltration instability[54]. Numerical modelling in two dimensions has suggested that such channels are created during reactive melt flow in the mantle[54,69,70], but their formation and importance in crustal mush reservoirs is not yet clear. Future work should investigate whether additional controls on flow in crustal magma reservoirs are observed in two- and three-dimensional models. Such models are likely to be computationally expensive.

The Boussinesq approximation is applied, so density differences between solid and liquid are neglected except for terms involving gravity[10,34,51]. Melt fraction and porosity are synonymous in this model. However, in contrast to previous models of crustal magma reservoirs, changes in local bulk composition resulting from melt migration mean that the local melt fraction here cannot be simply related via temperature to the melt fraction in the initial bulk composition (Extended Data Fig. 1c). This is a very important aspect of our model and one that pertains in both simple chemical systems (as employed here) and complex natural systems.

The governing equations can be expressed in dimensionless form as[10]

$$\frac{\partial h'}{\partial t'} = \kappa \frac{\partial^2 T'}{\partial z'^2} + \mathrm{Ste}\frac{\partial}{\partial z'}((1-\varphi)w_s') \tag{1}$$

$$\frac{\partial C}{\partial t'} = -\frac{\partial}{\partial z'}((1-\varphi)w_s' C_s) - \frac{\partial}{\partial z'}(\varphi w_m' C_m) \tag{2}$$

$$\frac{\partial I}{\partial t'} = -\frac{\partial}{\partial z'}((1-\varphi)w_s' I_s) - \frac{\partial}{\partial z'}(\varphi w_m' I_m) \tag{3}$$

$$\frac{\partial}{\partial z'}\left(\varphi^{-\beta}\frac{\partial w_s'}{\partial z'}\right) = \frac{\mu' w_s'}{\varphi^{\alpha}} + (1-\varphi)\Delta\rho' \tag{4}$$

$$\varphi w_m' = -(1-\varphi)w_s' \tag{5}$$

where h is the enthalpy per unit mass; T is the temperature; t is the time; z is the vertical coordinate; w is the velocity; φ is the melt fraction; C is the composition, defined using the phase diagram described in the next section; I is the trace-element concentration; $\Delta\rho$ is the density contrast between melt and crystals and μ is the melt shear viscosity, both discussed below. Subscripts 's' and 'm' denote solid and melt, respectively. Primes denote the dimensionless equivalents of the dimensional variables.

The characteristic timescales and length scales used to non-dimensionalize the equations are given by[10]

$$\tau = \frac{1}{\Delta\rho_r g}\left(\frac{\mu_r \eta_0}{a^2 b}\right)^{\frac{1}{2}} \tag{6}$$

$$\delta = \left(\frac{\eta_0 a^2 b}{\mu_r}\right)^{\frac{1}{2}} \tag{7}$$

where $\Delta\rho_r$ is a reference density contrast and μ_r a reference melt shear viscosity discussed in below, g is the acceleration due to gravity, and the matrix viscosity is related to the melt fraction by[10,34,50]

$$\frac{4}{3}\eta + \xi = \eta_0 \varphi^{-\beta} \tag{8}$$

where η is the shear viscosity, ξ is the bulk viscosity, η_0 is a reference shear viscosity and β is an adjustable constant. The permeability of the mush k_φ is given by[10,34,48,51]

$$k_\varphi = a^2 b \varphi^{\alpha} \tag{9}$$

where a is the grain size, and b and α are adjustable constants.

Temperature and enthalpy are scaled using[10]

$$T' = \frac{T - T_S}{T_L - T_S} \tag{10}$$

$$h' = \frac{h - h_S}{h_L - h_S} \tag{11}$$

where the subscripts 'L' and 'S' denote liquidus and solidus respectively. The dimensionless scaling factor κ in equation (1) is given by[10]

$$\kappa = \frac{k_T \tau (T_L - T_S)}{\rho_r \delta^2 (c_p (T_L - T_S) + L_f)} \quad (12)$$

and the Stefan Number by[10]

$$\mathrm{Ste} = \frac{L_f}{c_p (T_L - T_S) + L_f} \quad (13)$$

where k_T is the thermal diffusivity, c_p the sensible heat capacity, L_f the latent heat of fusion and ρ_r is a reference density discussed below.

The initial condition is chemically homogeneous crust with a constant linear geotherm T_{geo} and no melt present. Temperature, melt fraction and velocity are zero at the upper boundary (Earth surface); the lower boundary has constant T_{geo} and is set sufficiently deep that melt fraction and velocity remain zero. Equations (1)–(5) were solved numerically using finite difference methods and the MUSHREACT code that we developed. Equation (1) was approximated using a forward-time-centred-space scheme; equations (2) and (3) using a modified Lax–Wendroff scheme; and equation (4) using a centred scheme. Node spacing and time steps were chosen based on the results of convergence tests. Solutions reported here used 20–40 nodes per individual sill intrusion with time steps that were always less than the well known CFL condition[34,71].

The numerical methods and code have been validated extensively against analytical solutions[10,34,51,71]. The energy conservation equation (1) is a special case of the general parabolic diffusion–advection equation, while the mass conservation equations (2) and (3) are special cases of the general hyperbolic flux conservative equation. Analytical solutions are available for simplified forms of these general equations, and the numerical methods were tested against these. An analytical solution is available for a simplified set of the compaction equations and the code was also tested against this.

Phase behaviour and composition-dependent material properties. Phase change and compositions are described using a binary eutectic phase diagram that approximates the behaviour of natural systems. Several previous studies of crustal igneous systems have used a similar approach, which is preferable to more complex models involving, for example, the thermodynamic software MELTS[72] for two reasons. First, reactive flow leads to local changes in bulk composition, so the local phase equilibria must be recalculated at each location and time; this is trivial using a simple phase diagram, but computationally intensive (albeit possible) using MELTS. Second, it allows fundamental aspects of compositional evolution to be identified without the additional complexity associated with modelling the phase behaviour of natural systems[10,37].

Melt fraction is related to composition through

$$\varphi = \frac{C - C_s}{C_m - C_s} \quad (14)$$

where C is the local bulk composition. Assuming a linear release of enthalpy during melting, enthalpy is related to temperature through

$$h = c_p T + L_f \varphi \quad (15)$$

Using equations (14) and (15), and the temperature-dependent liquid and solid compositions determined from the phase diagram, the melt fraction is determined locally.

The binary eutectic phase diagram is described by a quadratic function given by[10]

$$C_m = \begin{cases} \dfrac{-a_2 - \sqrt{a_2^2 - 4a_1(a_3 - T)}}{2a_1} & C > e \\ \dfrac{-b_2 + \sqrt{b_2^2 - 4b_1(b_3 - T)}}{2b_1} & C < e \end{cases} \quad (16)$$

$$C_s = \begin{cases} 0 & C > e \\ 1 & C < e \end{cases} \quad (17)$$

Here, only compositions with $C < e$ were used. Values of the constants a_1, a_2 and a_3 were selected so that the melting relations obtained for starting compositions chosen to represent crust and intruded basalt match typical experimental data for the equilibrium melting/crystallization of metagreywackes and basalt, respectively, over the pressure range 400–900 MPa (Extended Data Fig. 1a; Extended Data Table 1)[12,73,74]. The match is surprisingly good given the simple phase behaviour adopted.

It is important to recognize that the static melt fraction versus temperature relations shown in Extended Data Fig. 1a are specific to the chosen starting bulk compositions. They are not valid if the bulk composition changes in response to reactive melt flow. The phase diagram provides a family of melting curves for all bulk compositions encountered in the reservoir; we show just two in Extended Data Fig. 1a. The effect of reactive melt flow in the reservoir is to decouple melt fraction and temperature (Extended Data Fig. 1c). High melt fraction can be found at low temperatures where reactive melt flow has caused the bulk composition of the mush to evolve towards the eutectic and vice versa. It is often assumed that high melt fraction necessitates high temperature[6–8,22,23,31–33,75]. Reactive melt flow means that this is not the case in crustal mush reservoirs.

We choose to relate composition C to a simple measure of differentiation, the SiO_2 content, by

$$S_{SiO_2} = a_5 + a_6 \tanh(a_7 + a_8 C) \quad (18)$$

Values of the constants a_5 to a_8 were selected to yield a variation in SiO_2 content with temperature that matches melt SiO_2 content from the same experimental melting/crystallization data (Extended Data Fig. 1b; Extended Data Table 1). Again, the match is surprisingly good given the simple phase behaviour adopted.

Rearrangement of equations (14), (16) and (17), followed by substitution into equation (15), yields a cubic polynomial in melt fraction, dependent on enthalpy h and bulk composition C, which can be solved analytically[10]

$$\varphi = \frac{h}{L_f} - \frac{c_p}{L_f}\left(\frac{a_3 + \left(\left(2a_1\left(\frac{C - C_s + C_s\varphi}{\varphi}\right) + a_2\right)^2 + a_2^2\right)}{4a_1}\right) \quad (19)$$

The model includes partitioning of a trace element between crystals and melt. The concentration in the melt is given by

$$I_m = \frac{I}{K + \varphi(1 - K)} \quad (20)$$

and in the solid by

$$I_s = K I_m \quad (21)$$

In the cases modelled here, the intruding magma and crust have the same initial concentration of an incompatible trace element. This is unlikely to occur in nature, but allows the evolution of trace-element concentration in response to reactive melt flow in the mush to be more clearly observed and understood. Trace-element concentration does not affect the evolution of temperature or melt fraction, so the other key model results remain unchanged.

The density of the melt and matrix, and the viscosity of the melt, both vary as a function of composition. Solid and melt densities are given by

$$\rho_m = C\rho_{m,min} + (1 - C)\rho_{m,max} \quad (22a)$$

$$\rho_s = C\rho_{s,min} + (1 - C)\rho_{s,max} \quad (22b)$$

where the subscripts 'max' and 'min' denote, respectively, the most evolved and least evolved (most refractory) compositions in the system. The average density of the crystals plus melt mixture (mush or magma) is given by

$$\bar{\rho} = \phi\rho_m + (1 - \phi)\rho_s \quad (23)$$

The dimensionless density is obtained by dividing by a reference density ρ_r chosen as the initial density of the crust, and the dimensionless density contrast is obtained by dividing by a reference density contrast $\Delta\rho_r$ chosen to be the difference in density between the most refractory crystals ($\rho_{s,max}$) and most evolved melt ($\rho_{m,min}$).

The logarithm of melt shear viscosity μ is linearly related to the dimensionless silica content of the melt s_{SiO_2}

$$\mu = 10^{((\mu_{max} - \mu_{min})S_{SiO_2} + \mu_{min})} \quad (24)$$

with

$$s_{SiO_2} = \frac{S_{SiO_2} - S_{SiO_2}^{min}}{S_{SiO_2}^{max} - S_{SiO_2}^{min}} \quad (25)$$

where S_{SiO_2} is the silica content of the melt (in weight per cent)[58]. The dimensionless melt shear viscosity is then obtained by dividing by a reference viscosity μ_r

chosen to be the maximum melt viscosity in the system (corresponding to the most evolved composition), to yield

$$\mu' = 10^{(\log(\mu_{min}/\mu_{max})(1-s_{SiO_2}))} \quad (26)$$

In the illustrative models shown here, melt viscosity varies from a minimum of 1 Pa s to a maximum of 10^5 Pa s (Extended Data Table 1) for the most mafic and most felsic compositions respectively, which is reasonable for melt containing a few weight per cent water[58]. A range of maximum melt viscosities is investigated in the sensitivity analysis described below.

Modelling of sill intrusion. The governing equations do not include terms representing addition of heat and mass in response to repetitive sill intrusion. Each sill intrusion is modelled numerically, using a simple approach in which new nodes, populated with the properties (enthalpy, melt fraction, major element composition and trace-element concentration) of the magma in the sill, are added into the model at the target intrusion depth[22,32,34]. The number of new nodes is chosen to yield the desired sill thickness. Pre-existing nodes below the location of sill intrusion are shifted downwards to accommodate the new nodes representing the sill; this approach represents, numerically, the way that intrusion of each new sill causes downward displacement of deeper crust and approximates isostatic equilibrium. Intrusion of each sill is assumed to occur over a timescale that is small compared to the thermal and chemical evolution of the magma reservoir and within a single time-step in the model. We note that injection of magma may generate local over-pressure, fracturing and, during the growing and active phases of the magma reservoir, locally disrupt the mush. Future refinements will focus on methods to better couple thermal and mechanical models.

Sill intrusion depth. Previous numerical studies have modelled repetitive intrusion by over-accretion, in which each new sill is intruded immediately above the previous sill; under-accretion, in which each new sill is intruded immediately below the previous sill; and random intrusion of sills and dykes around a fixed depth[21–23,32–34]. The approach used here to link sill intrusion depth to the state of the mush reservoir at the time of intrusion yields variations in intrusion depth that are not captured by these previous models.

Controls on the depth of sill intrusions include rigidity contrasts and rheology anisotropy, resulting from variations in lithology and (if present) melt fraction; rotation of deviatoric stress such that the minimum deviatoric stress becomes vertical; and density contrasts between the surrounding country rock and intruding magma[67,68]. The initial intrusion depth is chosen here to match the depth of an observed magma reservoir. Understanding why a sill should be initially emplaced at a given depth is beyond the scope of this Letter. Once the first sill is emplaced, the depth of subsequent intrusions is controlled by the density contrast between the intruding magma and the surrounding reservoir. The next sill intrusion occurs at the deepest level of the mush that has a lower bulk density (crystals plus melt) than the intruding magma. The top of the resulting reservoir tends to be close to the initial intrusion depth.

Density contrasts are controlled by the local composition and/or melt fraction of the mush reservoir. We use density contrasts here as a proxy for rigidity contrasts resulting from changes in rock composition or mush melt fraction[21,56,57,67,68]. Density is calculated using equations (22) and (23); the chosen values of density for refractory crystals ($\rho_{s,max}$) and most evolved melt ($\rho_{m,min}$) (Extended Data Table 1) yield densities of about 3,000 kg m^{-3} and about 2,600 kg m^{-3} for solid basalt and evolved (felsic) rock compositions respectively, and densities of about 2,800 kg m^{-3} and about 2,350 kg m^{-3} for their corresponding molten counterparts. These values are consistent with measured data[25,76,77]. The initial (reference) density of the solid crust is about 2,850 kg m^{-3}, consistent with data for intermediate rocks[77].

During the incubation phase, melt fraction falls to zero between successive sill intrusions (Extended Data Fig. 2), but variations in density arise in response to differentiation within each intruded sill as it cools. Differentiation yields a lower-density, evolved top and a higher-density, more refractory base (Extended Data Fig. 3a and Supplementary Video 1). Similar compositional trends are observed in sills now exposed at the surface[10,78,79]. The density-controlled intrusion depth of each new sill is, therefore, located below the deepest evolved top of a previous, now solidified, sill intrusion.

During the growing and active phases of the reservoir (Extended Data Fig. 2b), melt is persistently present and the compositional and density variations formed during the incubation phase are reduced by reactive melt flow (Fig. 1 and Supplementary Video 1). Variations in density are then primarily controlled by melt fraction, so that the density-controlled intrusion depth of each new sill is located below the deepest high melt fraction layer.

Field observations from deep crustal sections suggest that intrusions progressively accumulate to form a mush zone[16,21,76]. At early times, when the heat content of the reservoir is still low, intrusions cool without causing extensive melting of the surrounding crust, leaving septa of crust interleaved with the intruded sills. We model this by intruding sills at random over a range of 300 m above and below the intrusion depth determined by density contrast.

Random intrusion preserves septa of crustal rock between sill intrusions, whereas strictly density-controlled intrusion does not (see also Solano et al.[10]). Varying the depth range of random intrusion affects the frequency and volume of preserved septa, but does not otherwise substantially affect the results obtained. Although septa between early intrusions are preserved, septa between later intrusions, when the heat content of the reservoir is higher, are partially assimilated into the melt phase, causing crustal contamination of the melt[16,76,80,81].

Validity of the model at high melt fraction. The reactive flow and compaction formulation is applied in the model regardless of local melt fraction. However, it is strictly valid only when the crystals form a solid framework that will expel melt if it undergoes mechanical disruption or viscous deformation[82]. Estimates of the melt fraction at which this framework forms vary widely (over the range 0.4–0.7) and probably depend on local shear stresses and strain rates, and the crystal morphology and size distribution[40,45,82–84]. Melt fractions higher than this are present in each sill immediately after intrusion and in the melt layers that form in response to reactive flow. However, we argue below that the formulation captures enough of the physics to yield informative results.

High melt fractions are present in the intruding sills over very short timescales (of the order of hundreds of years) because the sills cool very rapidly, losing heat to the surrounding reservoir and/or crust (for example, Extended Data Fig. 2a). Over these short timescales following each intrusion, crystal–melt separation is assumed in the model to occur only by reactive flow and compaction, omitting other mechanisms of crystal-melt separation[82]; moreover, it is assumed that there is no bulk flow of melt and crystals driven by convection[28,85,86]. However, the modelled cooling timescale is correct, because the rate of heat loss from each sill is dominated by conduction and this is described by equation (1)[71,86]. Furthermore, in each sill, the model captures enough crystal–melt separation to yield a more evolved top, relatively enriched in incompatible trace elements, and a more refractory base, relatively depleted in incompatible trace elements, consistent with observations (for example, Fig. 3)[10,78,79].

High melt fractions are also present in the layers that form in response to reactive melt flow (for example, Fig. 1). These layers are persistently present once formed and the model again assumes that crystal–melt separation in each layer occurs only by reactive flow and compaction and that there is no bulk flow of melt and crystals driven by convection. However, the rate of delivery of new melt into the layer is controlled by reactive flow and compaction of the underlying mush where the formulation is valid. Moreover, the rate of upward movement of the layer, which affects cold storage, is controlled by the rate of upward movement of the solidus isotherm; this depends on conductive heat transfer in the overlying mush and solid rock, and is captured by the formulation. Thus we argue that the model captures the overall growth and upward migration of the layers.

Within each high-melt-fraction layer, the formulation probably does not correctly capture the variation in melt fraction. However, the modelled temperature in each layer is constant at the solidus; melt fraction is also high and approximately constant, controlled primarily by the local bulk composition (for example, Supplementary Video 1; Fig. 1). Thus, the modelled temperature and melt fraction assuming reactive flow with no bulk flow of melt and crystals are similar to what would be observed for the opposite end-member model of vigorous convection in which crystals are suspended and mixed in the magma[28]. We argue that vigorous convection may be more likely given the results of earlier studies of single sill intrusions[28,85,86].

Magma mobilization. Accumulation of melt creates a high-melt-fraction layer which, as it migrates upwards, can remobilize old mush by causing a rapid increase in melt fraction. The short timescale of this process may not allow for local chemical equilibrium to be maintained, so older crystals can be preserved in the younger magma. Disequilibrium between melt and crystals may also give rise to resorption and zonation of crystals which is not described here.

The model does not attempt to capture migration out of the reservoir of the high-melt-fraction (low-crystallinity) magmas in the layer. Felsic magma that accumulates at the top of the reservoir is buoyant relative to the surrounding mush reservoir, so there is a pressure gradient to drive ascent to higher crustal levels or eruption at the surface[25,26]. The magma in each sill also evolves during cooling to become more buoyant relative to the more refractory mush, which may drive ascent of less evolved magmas. Preliminary work, not reported here, suggests that removal of felsic magma accumulating in a high-melt-fraction layer at the top of the reservoir does not affect the formation of subsequent layers, so long as ongoing sill intrusions continue to supply new magma to the reservoir.

This preliminary work is not reported because the model does not yet include clearly defined criteria for magma removal and ascent. Moreover, we note that the presence of volatile species, such as H_2O, whose solubility is pressure-dependent, complicates phase relations and physical properties during magma ascent, and consequently is not considered here. Further work should determine the controls on mobilization and eruption of the low-crystallinity magmas present in crustal mush reservoirs. What is clear from the results obtained here is that the

compositions of low-crystallinity magmas that can leave the reservoir, regardless of how or why that happens, are bimodal. In our model, the melt composition evolves to the eutectic; in more chemically complex systems, melt composition will evolve to other low-variance states, such as cotectics or peritectics (reaction boundaries). In all cases, the effect is to buffer chemically the composition of accumulated melts, as recently suggested on the basis of phase-equilibrium experiments[87].

Magmatic systems at shallower depth. The results shown in Fig. 1 (and also in Supplementary Video 1 and Extended Data Fig. 3) illustrate the key processes occurring within a crustal mush reservoir and were obtained using values of the model parameters that are typical of crustal systems (Extended Data Table 1 and associated references). The initial intrusion depth was chosen to allow model results to be compared against a deep crustal section now exposed at the surface: the Upper Mafic Complex of the Ivrea-Verbano zone, Italy[16,21,76]. The complex is interpreted to represent about 8 km of basalt intruded into the crust over a few million years (that is, at intrusion rates of the order of a few millimetres a year). The top of the complex is interpreted to have been located at a depth of about 18 km at the time of formation.

The model results can explain a wide range of magmatic phenomena. However, we recognize that many of the magmatic systems that provide compelling evidence for these phenomena cannot be approximated by a model tuned specifically to match data from the Upper Mafic Complex. In particular, systems providing evidence for cold storage and compositional bimodality are often located at shallower levels in the crust[6–9]. Moreover, major- and trace-element and isotopic data for these systems suggest they may be supplied by magmas of more evolved composition than basalt[6–9,88]. In transcrustal magmatic systems[1] there are probably multiple zones of intrusion: primitive basalt magmas may form intrusions deep in the crust that generate more evolved magmas; these magmas ascend through the crust to form intrusion zones at shallower depths.

We test here whether similar results are obtained if the first sill is intruded at a depth of 10 km rather than 18 km. Numerous magmatic systems are observed in geophysical data at similar depth[2,4,5,38]. All model parameters are the same as used previously (Extended Data Table 1), except that we assume the initial geotherm is appropriate for thermally mature crust where, for example, a deeper magmatic zone has thermally primed the upper crust before the onset of shallower magmatism. Previous studies have shown that this is necessary to allow upper-crustal magmatic systems to form without a prohibitively long incubation period or unreasonably high rate of magma intrusion[23].

The results obtained are qualitatively similar to those observed at 18 km depth. There is an incubation period, during which the melt fraction rapidly falls to zero, with compositional contrasts formed by chemical differentiation within each sill intrusion before solidification, causing the intrusion depth to increase progressively (Supplementary Video 2; Extended Data Fig. 4a). During the growing phase, buoyant melt again migrates upwards through the mush and reactive melt flow reduces, or removes, early formed compositional contrasts, so that the intrusion depth becomes controlled by the locally varying melt fraction (Supplementary Video 2; Extended Data Fig. 5a).

During the active phase, the reservoir can again produce evolved, low-crystallinity magmas from the high-melt-fraction layer that forms beneath the solidus isotherm, close to the top of the reservoir (Supplementary Video 2; Extended Data Fig. 5b). When intrusion of new sills ends, the reservoir enters the waning phase (Supplementary Video 2; Extended Data Fig. 4b) until the mush has completely solidified.

Cold storage is again observed where upwardly migrating, evolved melt rapidly accumulates around older antecrysts derived from crystallization of early sills (Extended Data Fig. 6). In this shallower example, melt accumulation forms a low-crystallinity magma a few hundreds of years after the local temperature exceeds the solidus, but the magma contains antecrysts formed about 1.3 Myr earlier (Extended Data Fig. 6). Compositional bimodality is again observed, as magmas in the high-melt-fraction layers have evolved composition, but magmas in the sills shortly after intrusion have compositions close to that of the intruded basalt (Extended Data Fig. 7a). Thus, the key results are consistently observed in models of shallower magmatic systems created and sustained by basaltic magmatism.

Intrusion of more evolved magma. We now test whether similar results are obtained at 10 km if the intruding sills contain magma of intermediate (andesitic) rather than basaltic composition. All other model parameters are the same as used in the previous 10 km model (Extended Data Table 1). We do not model intrusion of rhyolite magma because our density-controlled intrusion depth model does not apply for rhyolite magma: density-controlled intrusion alone would suggest that rhyolite should mostly erupt. That evolved, low-density magmas often intrude rather than erupt has been a challenge to density-driven models of magma ascent and intrusion for many years[67,68].

Intrusion of intermediate-composition (about 61% SiO_2) magma yields qualitatively similar behaviour to that observed in response to intrusion of basaltic magma. The incubation, growing, active and waning phases of reservoir life are all observed and, during the active phase, a high-melt-fraction layer containing evolved (felsic) magma overlies a thicker, low-melt-fraction mush (for example, Extended Data Fig. 8). Older antecrysts are again rapidly remobilized by the arriving melt layer although, in this case, storage is 'cool' rather than 'cold': the temperature remains above the solidus, but the melt fraction remains low until the melt layer arrives. Whether crystals are kept in cold (sub-solidus) or cool (supra-solidus) conditions may be difficult to determine from crystal chemistry data, requiring accurate estimates of reservoir and solidus temperatures;[6–9] the key point is that the crystals are stored at low (non-eruptible) melt fraction, as opposed to 'warm storage' where the magma remains eruptible[18].

Compositional bimodality is again observed, but here the magma compositions are either evolved (felsic), reflecting melt accumulation in the upwardly migrating layer, or intermediate, reflecting the composition of the intruding magma (Extended Data Fig. 7b). In general, we suggest that crustal mush reservoirs deliver magmas with compositions that reflect either (1) low-variance states, such as eutectics, cotectics or peritectics (reaction boundaries)[87] or (2) the intruding magma that creates the reservoir.

Intrusion depth model. Numerical tests show that compositionally bimodal, low-crystallinity magmas are obtained regardless of whether the intrusion depth is modelled using our sill intrusion depth model or simple under- or over-accretion. 'Cold' (or at least 'cool') storage of crystals, in a non-eruptible state, is also observed (for example, Extended Data Fig. 9a, b), except when intrusion depth is modelled using simple over-accretion. Over-accretion cannot yield cold or cool storage of antecrysts formed as part of the same magmatic event, as persistent sill intrusion at the top of the magma reservoir causes the melt layer to migrate upwards and form in the overlying crust (for example, Extended Data Fig. 9c and d). The crystals here are rapidly mobilized by the arrival of the melt layer, but the history of the crystals and their genetic relationship with the magmatic event may be much more complex. However, simple over-accretion requires the magma supplying each sill to pass through the mush reservoir regardless of local melt fraction, rheology or density, which is inconsistent with available evidence and models[67,68]. We argue that our sill intrusion model better captures the effect of the local mush state on intrusion depth.

Sensitivity analysis. Extended Data Table 1 shows that crustal magma reservoirs are described by a broad range of material properties. Values of many of these are poorly constrained. A simple sensitivity analysis was used to confirm that the results obtained are typical.

Previous work has shown that solutions to equations (1)–(5) are largely dictated by the value of the dimensionless scaling factor[51,71] κ. The effect of varying the other dimensionless parameter Ste is much smaller. Other studies, confirmed by additional numerical experiments conducted here, have shown that, for a given depth of intrusion and initial geothermal gradient, the thermal impact of intruding sills is controlled by the intrusion rate, irrespective of the model used to choose the sill intrusion depth[22,23,32,33]. The chosen intrusion rate of 5 mm yr^{-1} for the example results shown here corresponds to the time-averaged magma productivity in arc settings simplified to a one-dimensional geometry[24]. We now explore a range of intrusion rates around this value, consistent with estimates for different crustal magmatic systems and previous studies[21–24,32–34].

A simple Monte Carlo analysis[89] shows that 90% of the calculated values of κ for typical crustal parameters lie within the range $0.028 < \kappa < 2{,}160$ ($-1.55 < \log\kappa < 3.335$; see Extended Data Fig. 10a). Numerical solutions were obtained for ten values of $\log\kappa$ sampled evenly over this range in log space, for a range of values of the sill intrusion rate, three different intrusion depths and basalt that is intruded to a maximum thickness of 20 km (Extended Data Table 1). The results are summarized in Extended Data Fig. 10b and c by plotting the incubation time (the time required to reach the end of the incubation phase and produce a persistent mush reservoir; see Extended Data Fig. 2b), the activation time (the time required to produce an active reservoir with a low-crystallinity felsic magma layer; see Extended Data Fig. 2b), the bulk composition of the mobile magmas (that is, magmas with melt fraction >0.7), and the 'cold storage time' of antecrysts at the top of the reservoir, as a function of sill intrusion rate for the different intrusion depths. The 'cold storage time' is the time elapsed between the last intrusion and the local melt fraction exceeding 0.7 at locations close to the top of the reservoir (see Fig. 2 and Extended Data Figs. 6, 8). The cold storage time reflects the likely range of crystal ages in magmas that have achieved melt fractions exceeding 0.7.

The incubation time scales with the reciprocal of the intrusion rate squared, q^{-2} (Extended Data Fig. 10b). The same scaling has been obtained in previous, purely thermal, models of repetitive sill intrusion using a variety of intrusion depth schemes, showing that the incubation time is relatively insensitive to the details of sill intrusion[22,23,90]. Varying the value of κ over the range specified has a negligible impact on the incubation time, regardless of intrusion rate or depth, reflecting the relatively small range of uncertainty in thermal parameters such as thermal conductivity, specific heat capacity and latent heat (Extended Data Table 1).

The impact of varying κ on the accumulation time is larger, especially at lower intrusion rates when the accumulation time may be several million years longer than the incubation time (Extended Data Fig. 10b). Longer incubation times are observed for large values of κ that correspond to larger values of the melt shear viscosity and smaller values of matrix grain size, and for small values of κ that correspond to large values of the matrix bulk viscosity (Extended Data Table 1). Nevertheless, the accumulation time is finite so long as the incubation time is reached within the maximum intruded thickness of basalt; in other words, the formation of a high-melt-fraction layer is inevitable, so long as a persistent mush reservoir is present.

The composition of the high-melt-fraction (eruptible) magma in the reservoir is always bimodal, irrespective of the value of κ, the intrusion rate or intrusion depth (Extended Data Fig. 10c). The magma in the intruded sills has a composition close to that of the intruding basalt, while the magma in the layer that accumulates at the top of the reservoir has an evolved (approximately eutectic) composition, consistent with the results shown earlier for specific cases (Fig. 3; Extended Data Fig. 7a).

The impact of varying κ on the cold storage time is larger, as is the effect of intrusion rate (Extended Data Fig. 10c). Smaller cold storage times are observed for larger values of κ that correspond to larger values of the melt shear viscosity and smaller values of matrix grain size (Extended Data Table 1). Smaller cold storage times are also observed for higher intrusion rates, because evolution of the system as a whole occurs more rapidly. The cold storage time reflects the relative timing of sill intrusion relative to remobilization. Nevertheless, the cold storage time is always non-zero; in other words, some antecrysts are stored in a cold (or cool), non-eruptible state, before remobilization by reactive flow.

Code availability. The code (MUSHREACT) used to solve equations (1)–(5) and produce the results reported here is available from the corresponding author on request. The code is platform-dependent and is not optimized or tested for broad distribution, but the methodology is described within the article and preceding studies[10,34].

Data availability

No original data are reported that were not created using the software code (MUSHREACT). Data can be recreated using the code.

31. Hodge, D. S. Thermal model for origin of granitic batholiths. *Nature* **251**, 297–299 (1974).
32. Petford, N. & Gallagher, K. Partial melting of mafic (amphibolitic) lower crust by periodic influx of basaltic magma. *Earth Planet. Sci. Lett.* **193**, 483 (2001).
33. Dufek, J. & Bergantz, G. Lower crustal magma genesis and preservation: a stochastic framework for the evaluation of basalt–crust interaction. *J. Petrol.* **46**, 2167–2195 (2005).
34. Solano, J. M. S., Jackson, M. D., Sparks, R. S. J., Blundy, J. D. & Annen, C. Melt segregation in deep crustal hot zones: a mechanism for chemical differentiation, crustal assimilation and the formation of evolved magmas. *J. Petrol.* **53**, 1999–2026 (2012).
35. Bowen, N. L. *Evolution of the Igneous Rocks* 2nd edn, **362** (Dover, New York, 1956).
36. Hallworth, M. A., Huppert, H. E. & Woods, A. W. Crystallization and layering induced by heating a reactive porous medium. *Geophys. Res. Lett.* **31**, L13605 (2004).
37. Kerr, R. C., Woods, A. W., Grae Worster, M. & Huppert, H. E. Disequilibrium and macrosegregation during solidification of a binary melt. *Nature* **340**, 357–362 (1989).
38. Heise, W. et al. Melt distribution beneath a young continental rift: the Taupo Volcanic Zone, New Zealand. *Geophys. Res. Lett.* **34**, L14313 (2007).
39. Bachmann, O. & Bergantz, G. W. On the origin of crystal-poor rhyolites: extracted from batholithic crystal mushes. *J. Petrol.* **45**, 1565–1582 (2004).
40. Costa, A., Caricchi, L. & Bagdassarov, N. A model for the rheology of particle-bearing suspensions and partially molten rocks. *Geochem. Geophys. Geosyst.* **10**, Q03010 (2009).
41. Wolf, M. B. & Wyllie, P. J. Dehydration-melting of solid amphibolite at 10 kbar: Textural development, liquid interconnectivity and applications to the segregation of magmas. *Mineral. Petrol.* **44**, 151–179 (1991).
42. Ducea, M. N., Otamendi, J., Bergantz, G. W., Jianu, D. & Petrescu, L. in *Geodynamics of a Cordilleran Orogenic System: The Central Andes of Argentina and Northern Chile* (eds DeCelles, P. G. et al.) Geological Society of America Memoir Vol. 212, 125–138 (GSA, 2015).
43. Yoshino, T. & Okudaira, T. Crustal growth by magmatic accretion constrained by metamorphic P-T paths and thermal models of the Kohistan arc, NW Himalayas. *J. Petrol.* **45**, 2287–2302 (2004).
44. Hacker, B. R. et al. Reconstruction of the Talkeetna intraoceanic arc of Alaska through thermobarometry. *J. Geophys. Res.* **113**, B03204 (2008).
45. Rosenberg, C. L. & Handy, M. R. Experimental deformation of partially melted granite revisited: implications for the continental crust. *J. Metamorph. Geol.* **23**, 19 (2005).
46. Dell'Angelo, L. N., Tullis, J. & Yund, R. A. Transition from dislocation creep to melt-enhanced diffusion creep in fine-grained granitic aggregates. *Tectonophysics* **139**, 325–332 (1987).
47. Mei, S., Bai, W., Hiraga, T. & Kohlstedt, D. L. Influence of melt on the creep behavior of olivine-basalt aggregates under hydrous conditions. *Earth Planet. Sci. Lett.* **201**, 491–507 (2002).
48. McKenzie, D. P. The generation and compaction of partially molten rock. *J. Petrol.* **25**, 713–765 (1984).
49. Richter, F. M. & McKenzie, D. Dynamical models for melt segregation from a deformable matrix. *J. Geol.* **92**, 729–740 (1984).
50. Connolly, J. A. D. & Podladchikov, Y. Y. Compaction driven fluid flow in viscoelastic rock. *Geodin. Acta* **11**, 55–84 (1998).
51. Jackson, M. D., Cheadle, M. J. & Atherton, M. P. Quantitative modeling of granitic melt generation and segregation in the continental crust. *J. Geophys. Res.* **108**, 2332–2353 (2003).
52. Hersum, T. G., Marsh, B. D. & Simon, A. C. Contact partial melting of granitic country rock, melt segregation, and re-injection as dikes into ferrar dolerite sills, McMurdo dry valleys, Antarctica. *J. Petrol.* **48**, 2125 (2007).
53. Jackson, M. D., Gallagher, K., Petford, N. & Cheadle, M. J. Towards a coupled physical and chemical model for tonalite–trondhjemite–granodiorite magma formation. *Lithos* **79**, 43 (2005).
54. Keller, T., Katz, R. F. & Hirschmann, M. M. Volatiles beneath mid-ocean ridges: deep melting, channelised transport, focusing, and metasomatism. *Earth Planet. Sci. Lett.* **464**, 55–68 (2017).
55. Katz, R. F. Magma dynamics with the enthalpy method: benchmark solutions and magmatic focusing at mid-ocean ridges. *J. Petrol.* **49**, 2099–2121 (2008).
56. Ranalli, G. *Rheology of the Earth: Deformation and flow processes in Geophysics and Geodynamics* 2nd edn, 366 (Allen and Unwin, London, 1987).
57. Schmeling, H., Kruse, J. P. & Richard, G. Effective shear and bulk viscosity of partially molten rock based on elastic moduli theory of a fluid filled poroelastic medium. *Geophys. J. Int.* **190**, 1571–1578 (2012).
58. Giordano, D., Russell, J. K. & Dingwell, D. B. Viscosity of magmatic liquids: A model. *Earth Planet. Sci. Lett.* **271**, 123–134 (2008).
59. Bercovici, D., Ricard, Y. & Schubert, G. A two-phase model for compaction and damage. Part 1: general theory. *J. Geophys. Res.* **106**, 8887–8906 (2001).
60. Ricard, Y., Bercovici, D. & Schubert, G. A two-phase model for compaction and damage. Part 2: applications to compaction, deformation and the role of interfacial surface tension. *J. Geophys. Res.* **106**, 8907–8924 (2001).
61. Šrámek, O., Ricard, Y. & Bercovici, D. Simultaneous melting and compaction in deformable two-phase media. *Geophys. J. Int.* **168**, 964–982 (2007).
62. Simpson, G., Spiegelman, M. & Weinstein, M. I. A multiscale model of partial melts: 1. Effective equations. *J. Geophys. Res.* **115**, B04410 (2010).
63. Khazan, Y. Melt segregation and matrix compaction: the mush continuity equation, compaction/segregation time, implications. *Geophys. J. Int.* **183**, 601–610 (2010).
64. Karlstrom, L., Dufek, J. & Manga, M. Magma chamber stability in arc and continental crust. *J. Volcanol. Geotherm. Res.* **190**, 249–270 (2010).
65. Parmigiani, A., Faroughi, S., Huber, C., Bachmann, O. & Su, Y. Bubble accumulation and its role in the evolution of magma reservoirs in the upper crust. *Nature* **532**, 492–495 (2016).
66. Huppert, H. E. & Woods, A. W. The role of volatiles in magma chamber dynamics. *Nature* **420**, 493–495 (2002).
67. Menand, T. Physical controls and depth of emplacement of igneous bodies: a review. *Tectonophysics* **500**, 11–19 (2011).
68. Kavanagh, J. L., Boutelier, D. & Cruden, A. R. The mechanics of sill inception, propagation and growth: experimental evidence for rapid reduction in magmatic overpressure. *Earth Planet. Sci. Lett.* **421**, 117–128 (2015).
69. Spiegelman, M., Kelemen, P. & Aharonov, E. Causes and consequences of flow organization during melt transport: the reaction infiltration instability in compactible media. *J. Geophys. Res.* **106**, 2061–2077 (2001).
70. Liang, Y., Schiemenz, A., Hesse, M. A. & Parmentier, E. M. Waves, channels, and the preservation of chemical heterogeneities during melt migration in the mantle. *Geophys. Res. Lett.* **38**, L20308 (2011).
71. Jackson, M. D. & Cheadle, M. J. A continuum model for the transport of heat, mass and momentum in a deformable, multicomponent mush, undergoing solid-liquid phase change. *Int. J. Heat Mass Transfer* **41**, 1035–1048 (1998).
72. Ghiorso, M. S. & Sack, R. O. Chemical mass transfer in magmatic processes IV. A revised and internally consistent thermodynamic model for the interpolation and extrapolation of liquid-solid equilibria in magmatic systems at elevated temperatures and pressures. *Contrib. Mineral. Petrol.* **119**, 197–212 (1995).
73. Vielzeuf, D. & Montel, J. M. Partial melting of metagreywackes. Part I: fluid-absent experiments and phase relationships. *Contrib. Mineral. Petrol.* **117**, 375–393 (1994).
74. Blatter, D. L., Sisson, T. W. & Ben Hankins, W. Crystallization of oxidized, moderately hydrous arc basalt at mid- to lower-crustal pressures: implications for andesite genesis. *Contrib. Mineral. Petrol.* **166**, 861–886 (2013).
75. Burgisser, A. & Bergantz, G. W. A rapid mechanism to remobilize and homogenize highly crystalline magma bodies. *Nature* **471**, 212–215 (2011).
76. Sinigoi, S., Quick, J. E., Mayer, A. & Demarchi, G. Density-controlled assimilation of underplated crust, Ivrea-Verbano Zone, Italy. *Earth Planet. Sci. Lett.* **129**, 183–191 (1995).
77. Murase, T. & McBirney, A. R. Properties of some common igneous rocks and their melts at high temperatures. *Geol. Soc. Am. Bull.* **84**, 3563–3592 (1973).
78. Gibb, F. G. F. & Henderson, C. M. B. Convection and crystal settling in sills. *Contrib. Mineral. Petrol.* **109**, 538–545 (1992).
79. Latypov, R. M. The origin of basic– ultrabasic sills with S-, D-, and I-shaped compositional profiles by in-situ crystallization of a single input of phenocryst-poor parental magma. *J. Petrol.* **44**, 1619–1656 (2003).
80. Hildreth, W. & Moorbath, S. Crustal contributions to arc magmatism in the Andes of Central Chile. *Contrib. Mineral. Petrol.* **98**, 455 (1988).

81. Sisson, T. W., Salters, V. J. M. & Larson, P. B. Petrogenesis of Mount Rainier andesite: magma flux and geologic controls on the contrasting differentiation styles at stratovolcanoes of the southern Washington Cascades. *Geol. Soc. Am. Bull.* **126**, 122–144 (2014).
82. Holness, M. B. Melt segregation from silicic mushes: a critical appraisal of possible mechanisms and their microstructural record. *Contrib. Mineral. Petrol.* **173**, 48 (2018).
83. Philpotts, A. R. & Dickson, L. D. The formation of plagioclase chains during convective transfer in basaltic magma. *Nature* **406**, 59–61 (2000).
84. Castruccio, A., Rust, A. & Sparks, R. S. J. Rheology and flow of crystal-rich bearing lavas: insights from analogue gravity currents. *Earth Planet. Sci. Lett.* **297**, 471–480 (2010).
85. Worster, G. M., Huppert, H. E. & Sparks, R. S. J. Convection and crystallization in magma cooled from above. *Earth Planet. Sci. Lett.* **101**, 78–89 (1990).
86. Bergantz, G. W. & Dawes, R. in *Magmatic Systems* (ed. Ryan, M. P.) Ch. 13 (Academic, San Diego, 1994).
87. Blatter, D. L., Sisson, T. W. & Ben Hankins, W. Voluminous arc dacites as amphibole reaction-boundary liquids. *Contrib. Mineral. Petrol.* **172**, 27 (2017).
88. Till, C. B., Vazquez, J. A. & Boyce, J. W. Months between rejuvenation and volcanic eruption at Yellowstone caldera, Wyoming. *Geology* **43**, 695–698 (2015).
89. Sobol, I. M. *A Primer for the Monte Carlo Method* 1st edn, 126 (CRC Press, 1994).
90. Michaut, C. & Jaupart, C. Ultra-rapid formation of large volumes of evolved magma. *Earth Planet. Sci. Lett.* **250**, 38–52 (2006).

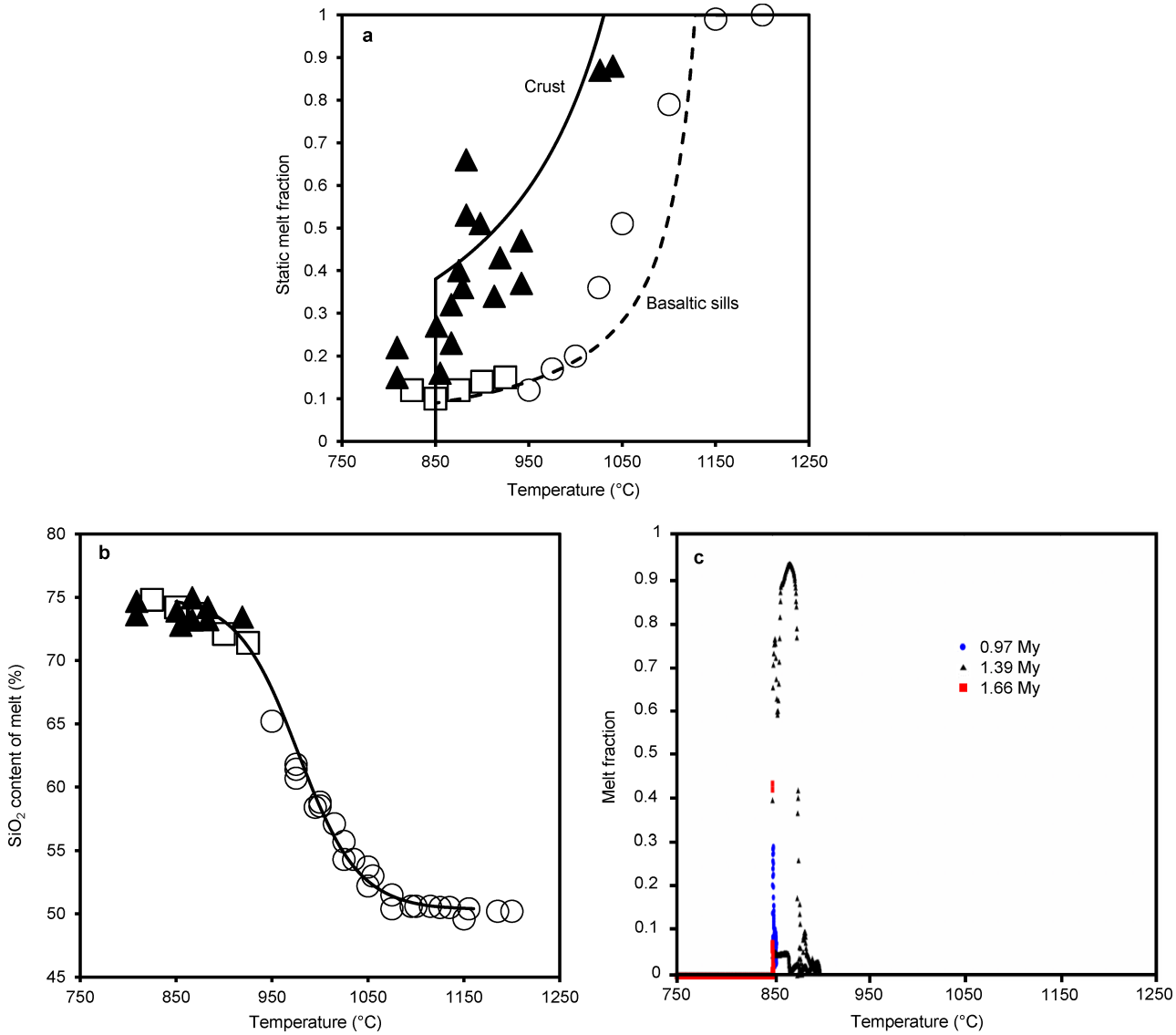

Extended Data Fig. 1 | Phase behaviour and compositions of the modelled system. a, Static melt fraction versus temperature for the modelled basalt and crust, extracted from the binary phase diagram for the chosen initial bulk compositions. Also shown are experimental equilibrium melting/crystallization data for metagreywackes and basalt over the pressure range[12,73,74] 400–900 MPa. Triangles denote data from ref. [73]; circles denote data from ref. [74]; squares denote data from ref. [12]. Static melt fraction denotes the melt fraction obtained if there is no relative motion of melt and crystals, so the bulk composition remains constant. **b**, SiO_2 content versus temperature modelled here. Also shown are experimental data corresponding to those shown in **a**. **c**, Melt fraction versus temperature obtained from the numerical model (data extracted from Supplementary Video 1 at three snapshots in time (0.97 Myr, 1.39 Myr and 1.66 Myr after the onset of sill intrusions) corresponding to Fig. 1 and Extended Data Fig. 3b. Reactive flow in the mush decouples temperature and melt fraction: high melt fraction can be found at low temperatures where reactive melt flow has caused the bulk composition of the mush to evolve and vice versa.

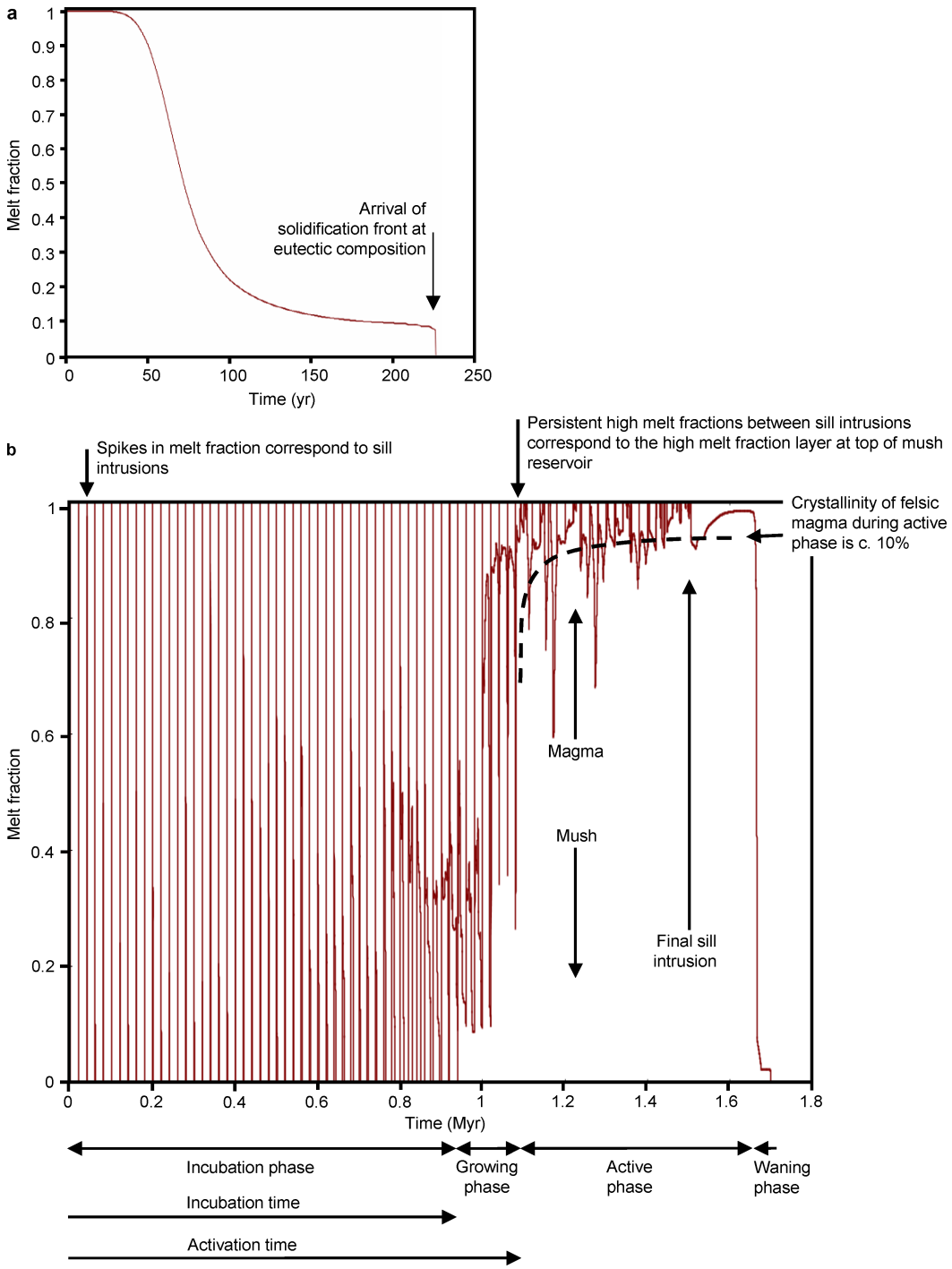

Extended Data Fig. 2 | Maximum melt fraction as a function of time. **a**, Following a single sill intrusion during the incubation period. **b**, Over the life of the reservoir. In **a**, the sill cools rapidly, with the melt fraction falling below 0.7 (that is, the crystallinity exceeding 30%) within 63 years after intrusion, and the sill solidifying within 225 years. The sharp decrease in melt fraction before full solidification is physical and represents the arrival of the solidification front during crystallization at the eutectic. In **b**, during the 'incubation phase', maximum melt fraction spikes after each sill intrusion, but decreases rapidly and falls to zero between sill intrusions. The incubation phase ends when the melt fraction remains greater than zero between sill intrusions. During the 'growing phase', the maximum melt fraction at the top of the mush reservoir increases in response to the reactive flow of buoyant melt. Spikes in melt fraction correspond to ongoing sill intrusions deeper in the reservoir. Melt fraction at the top of the mush increases until, during the 'active phase', evolved, low-crystallinity (<30%) magma is present, which is likely to leave rapidly and ascend to shallower crustal levels. New sill intrusions cease and, some time later, the melt fraction at the top of the mush also starts to decrease. Overall, the reservoir is cooling. This is the 'waning phase', at the end of which the reservoir has completely solidified. Data in both plots were extracted from Supplementary Video 1.

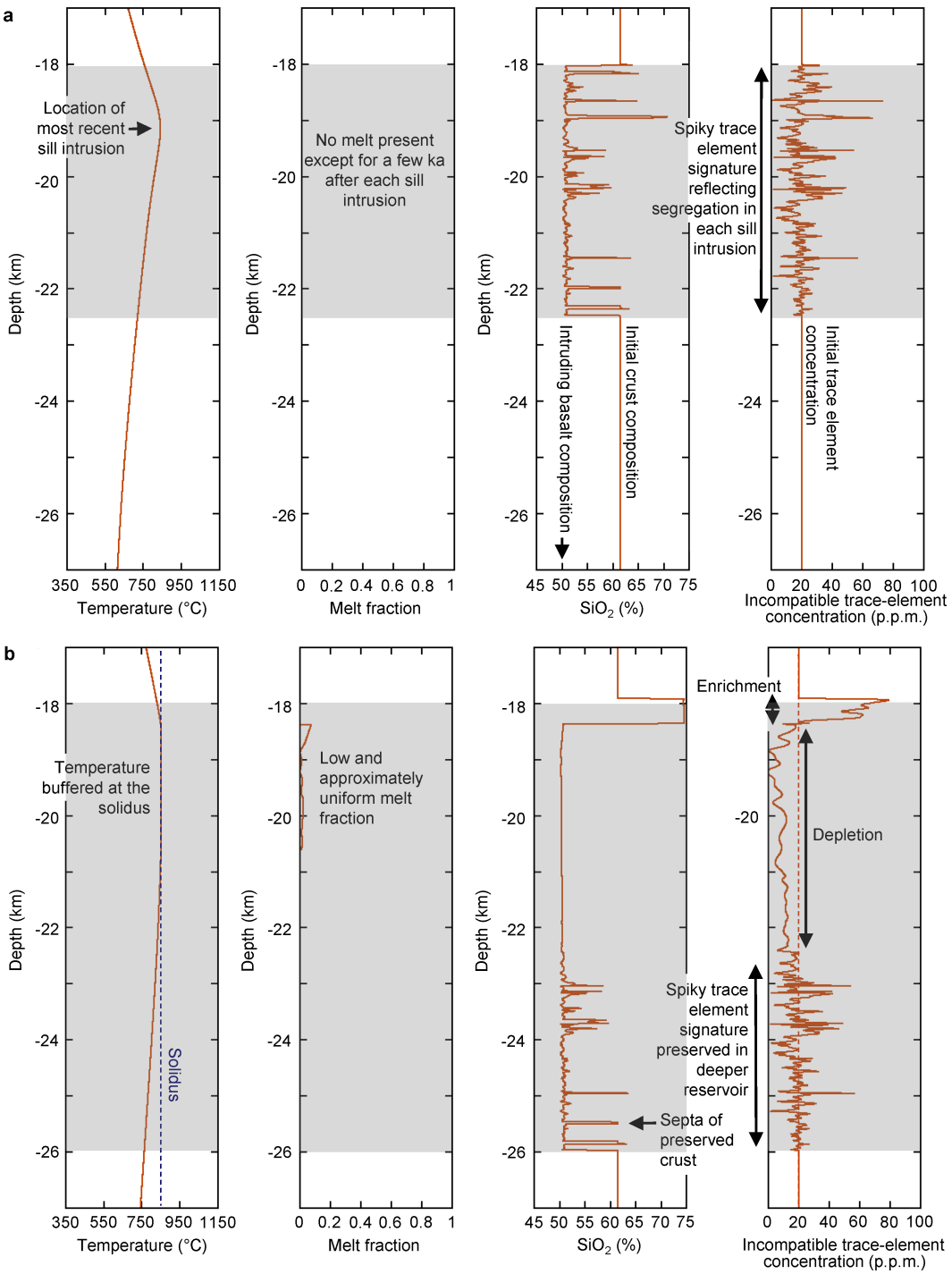

Extended Data Fig. 3 | Snapshots showing temperature, melt fraction, bulk composition and incompatible trace-element concentration as a function of depth through a crustal section at 18 km during the incubation and waning phases of the reservoir. a, 0.82 Myr after the onset of sill intrusions. **b**, 1.66 Myr after the onset of sill intrusions. Snapshots are taken from Supplementary Video 1. At early times, during the incubation phase (**a**), individual sills cool rapidly. During the growing phase (not shown here; see Fig. 1a), a persistent magma reservoir forms but the melt fraction is low and relatively uniform. However, buoyant melt migrates upwards and begins to accumulate at the top of the reservoir. During the active phase (not shown here; see Fig. 1b), a high-melt-fraction layer forms. At late times, during the waning phase (**b**), sill intrusions cease and the mush cools and solidifies. The shaded areas in all plots denote the vertical extent of basalt intrusion at that time. Equivalent results for intrusions at 10 km depth are shown in Extended Data Fig. 4.

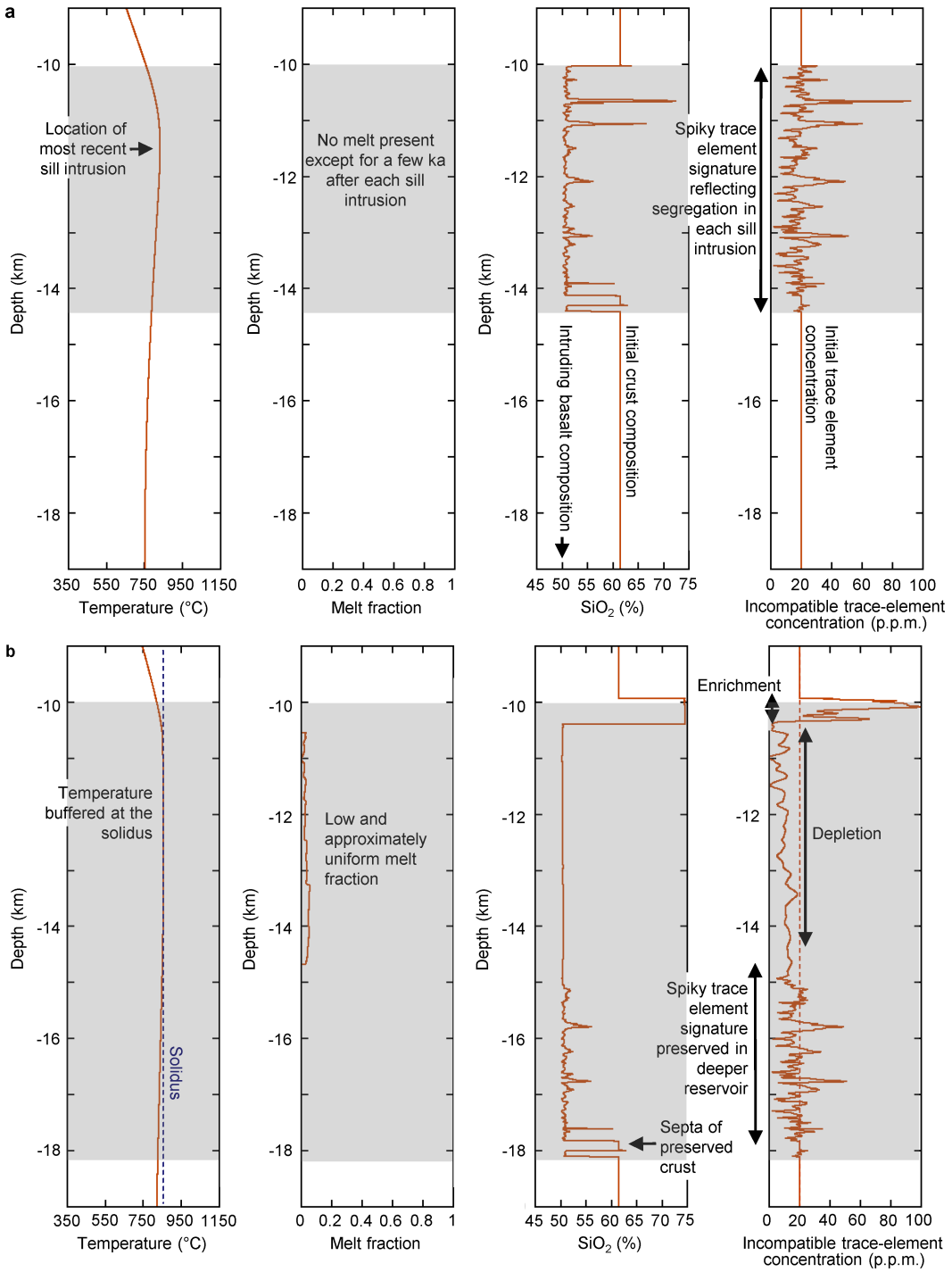

Extended Data Fig. 4 | Snapshots showing temperature, melt fraction, bulk composition and incompatible trace-element concentration as a function of depth through a crustal section at 10 km depth during the incubation and waning phases. a, 0.82 Myr after the onset of sill intrusions. **b**, 1.66 Myr after the onset of sill intrusions. Snapshots are taken from Supplementary Video 2. The results are qualitatively very similar to those obtained at 18 km depth (Extended Data Fig. 3). During the incubation phase (**a**), individual sills cool rapidly. During the waning phase (**b**), sill intrusions cease and the mush cools and solidifies. The shaded areas in all plots denote the vertical extent of basalt intrusion at that time.

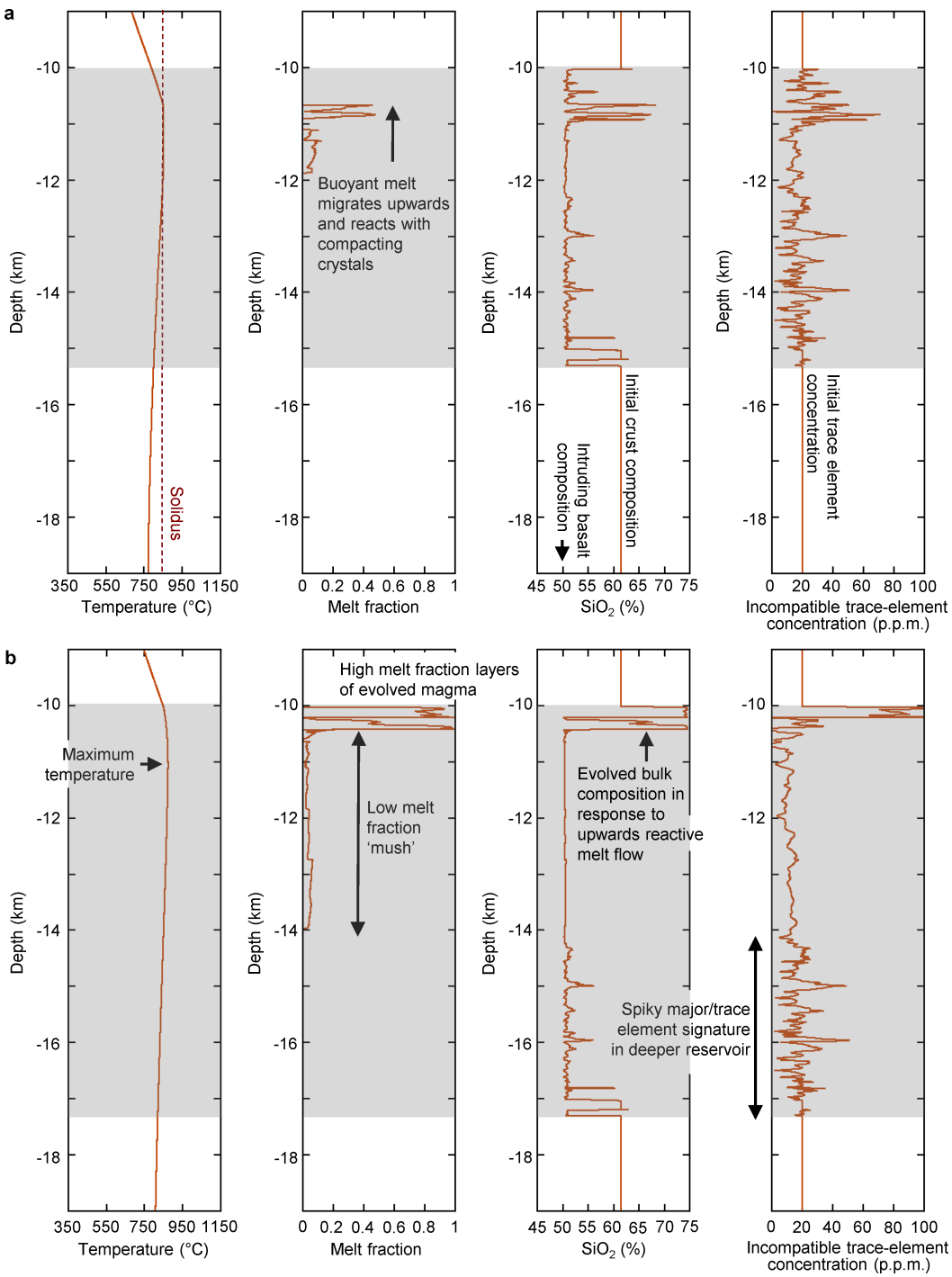

Extended Data Fig. 5 | Snapshots showing temperature, melt fraction, bulk composition and incompatible trace element concentration as a function of depth through a crustal section at 10 km depth during the growing and active phases. a, 0.99 Myr after the onset of sill intrusions. **b**, 1.39 Myr after the onset of sill intrusions. Snapshots are taken from Supplementary Video 2. The results are qualitatively very similar to those obtained at 18 km depth (Fig. 1). During the growing phase (**a**), a persistent mush reservoir forms but the melt fraction is low. Buoyant melt migrates upwards and begins to accumulate at the top of the reservoir. During the active phase (**b**), the accumulating melt forms a high-melt-fraction layer containing mobile magma. The composition of the melt in the layer is evolved and enriched in incompatible trace elements. Elsewhere in the mush, the melt fraction remains low. The shaded areas in all plots denote the vertical extent of basalt intrusions at that time.

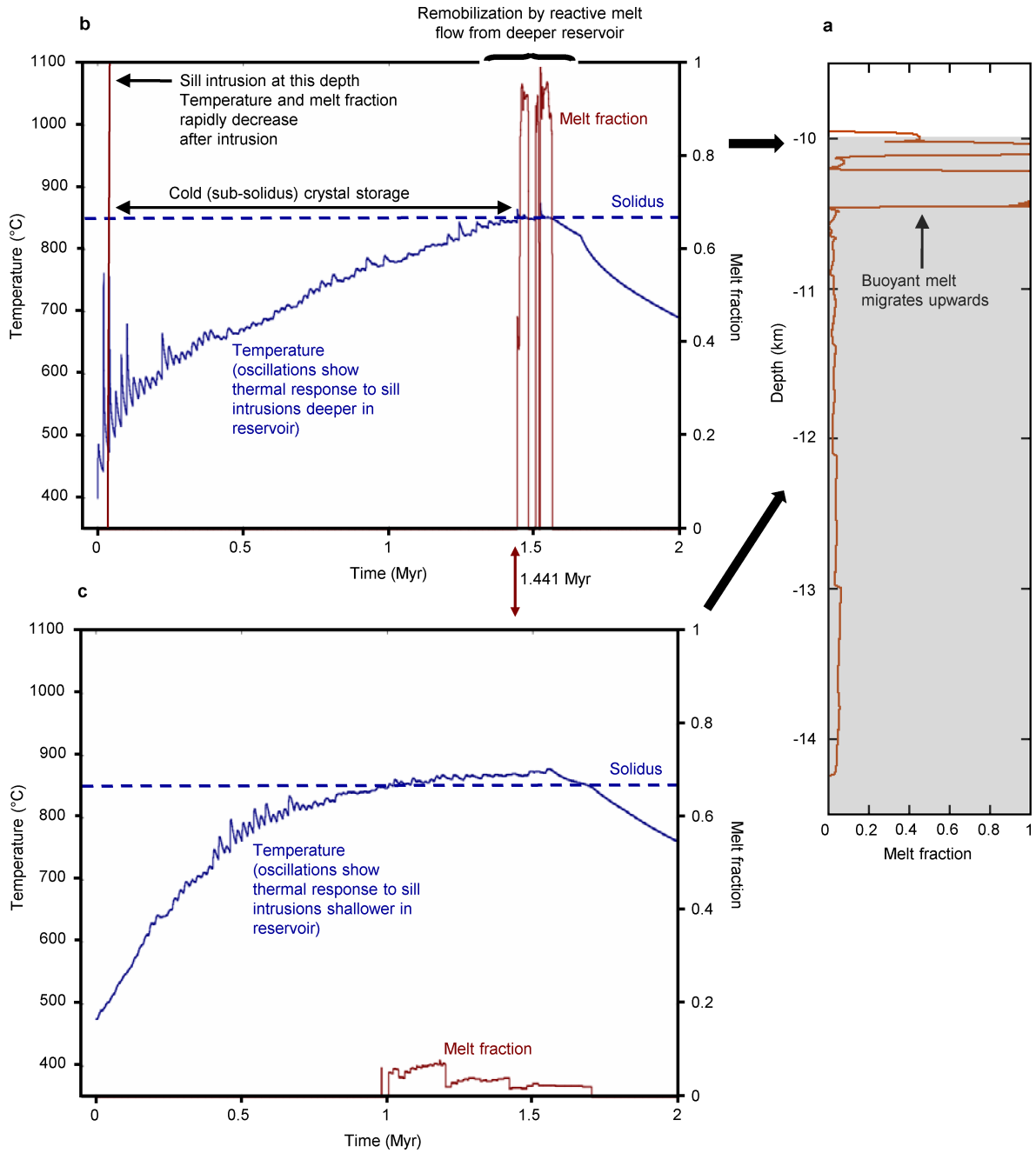

Extended Data Fig. 6 | Cold storage and rapid remobilization of magma in a reservoir at 10 km depth. Results are qualitatively very similar to those obtained at 18 km depth (Fig. 2). **a**, Melt fraction as a function of depth at the first snapshot after remobilization at 10 km (1.441 Myr after the onset of sill intrusions). The shaded area denotes intruded basalt. The reactive flow of buoyant melt produces a high-melt-fraction layer that migrates upwards. **b**, Temperature and melt fraction as a function of time at a depth of 10 km. Similar results are obtained over the depth range 10–10.5 km. Early sill intrusions rapidly cool and crystallize. The crystals are kept in 'cold storage' at sub-solidus temperature, but the temperature gradually increases in response to sill intrusions deeper in the reservoir. Soon (<0.3 kyr) after the temperature exceeds the solidus, the high-melt-fraction layer arrives at this depth and the reservoir is remobilized: the melt fraction increases rapidly to form a low-crystallinity magma. The melt fraction increases much more rapidly and to a higher value than would be possible by melting alone. **c**, Temperature and melt fraction as a function of time at a depth of 12 km. Similar results are obtained over the depth range 10.5–15 km. Melt fraction remains low because reactive flow has left a refractory residue at this depth. There is no remobilization, despite the increase in temperature. Data were extracted from Supplementary Video 2.

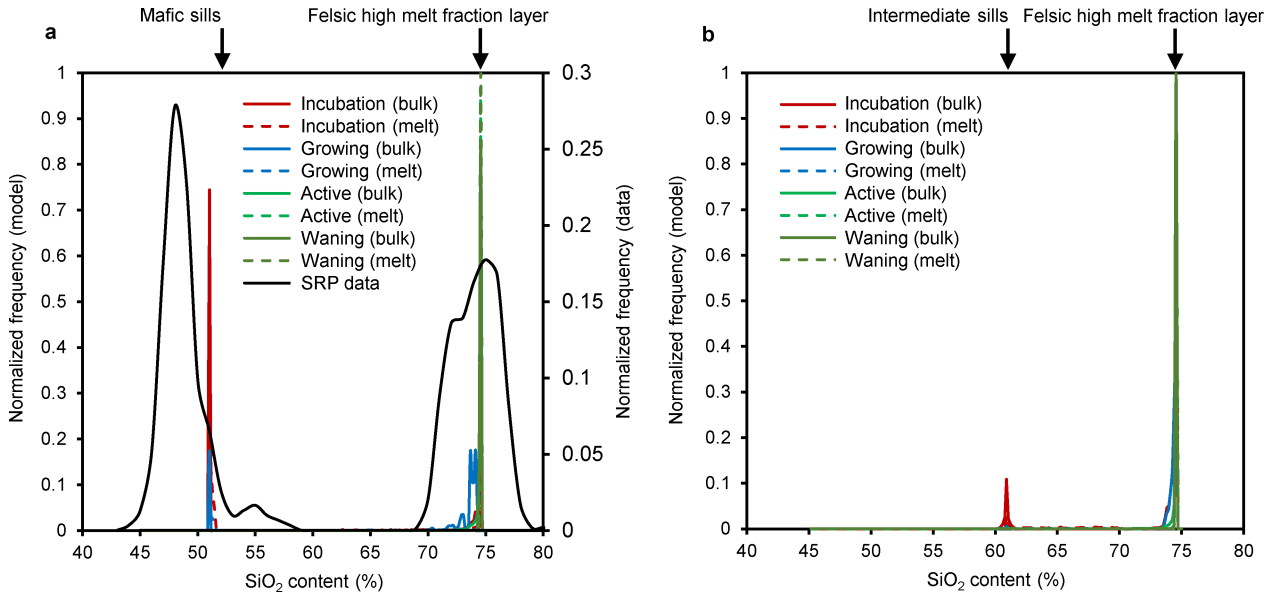

Extended Data Fig. 7 | Geochemical consequences of reactive melt flow in crustal magma reservoirs at 10 km depth. a, Intrusion of mafic sills; **b**, intrusion of intermediate sills. Both plots show SiO_2 content of low-crystallinity (crystal fraction <30%) magmas. Solid curves show bulk magma composition (melt plus crystals); dashed curves show melt composition alone. The peak at low SiO_2 corresponds to magma within the intruding sills; the peak at high SiO_2 corresponds to magma within high-melt-fraction layers near the top of the reservoir. In **a**, measured data from the Snake River Plain (SRP) are shown for comparison[29]; the bimodality is clear although the basalt has a lower SiO_2 content than modelled here. Bimodal compositions correspond to (1) the magma intruded into the reservoir, and (2) the most evolved composition obtained by differentiation.

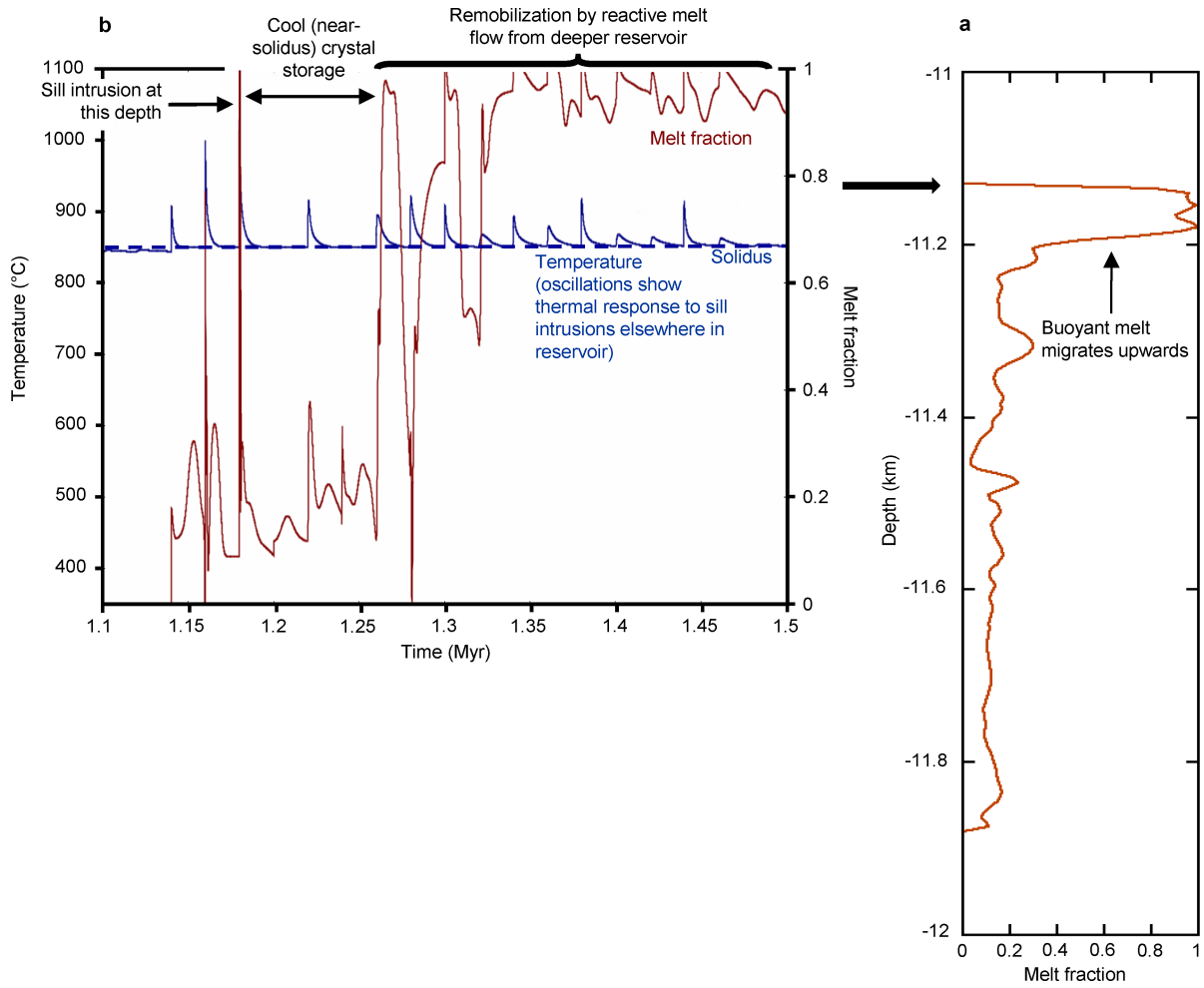

Extended Data Fig. 8 | Cool storage and rapid remobilization of magma in a reservoir created by intrusion of intermediate magma at 10 km depth. Results are qualitatively similar to those obtained by intruding basalt magma. **a**, Melt fraction as a function of depth at the first snapshot after remobilization at a depth of 11.4 km (1.28 Myr after the onset of sill intrusions). Reactive flow of evolved, buoyant melt produces a high-melt-fraction layer that migrates upwards. **b**, Temperature and melt fraction as a function of time at a depth of 11.4 km. Early sill intrusions rapidly cool and crystallize. The crystals are kept in 'cool storage' at near-solidus temperature. At 1.28 Myr, the high-melt-fraction layer arrives at this depth and the reservoir is remobilized: the melt fraction increases rapidly to form a low-crystallinity magma. The melt fraction increases much more rapidly and to a higher value than would be possible by melting alone. Melt fraction deeper in the reservoir remains low because reactive flow has left a refractory residue at this depth.

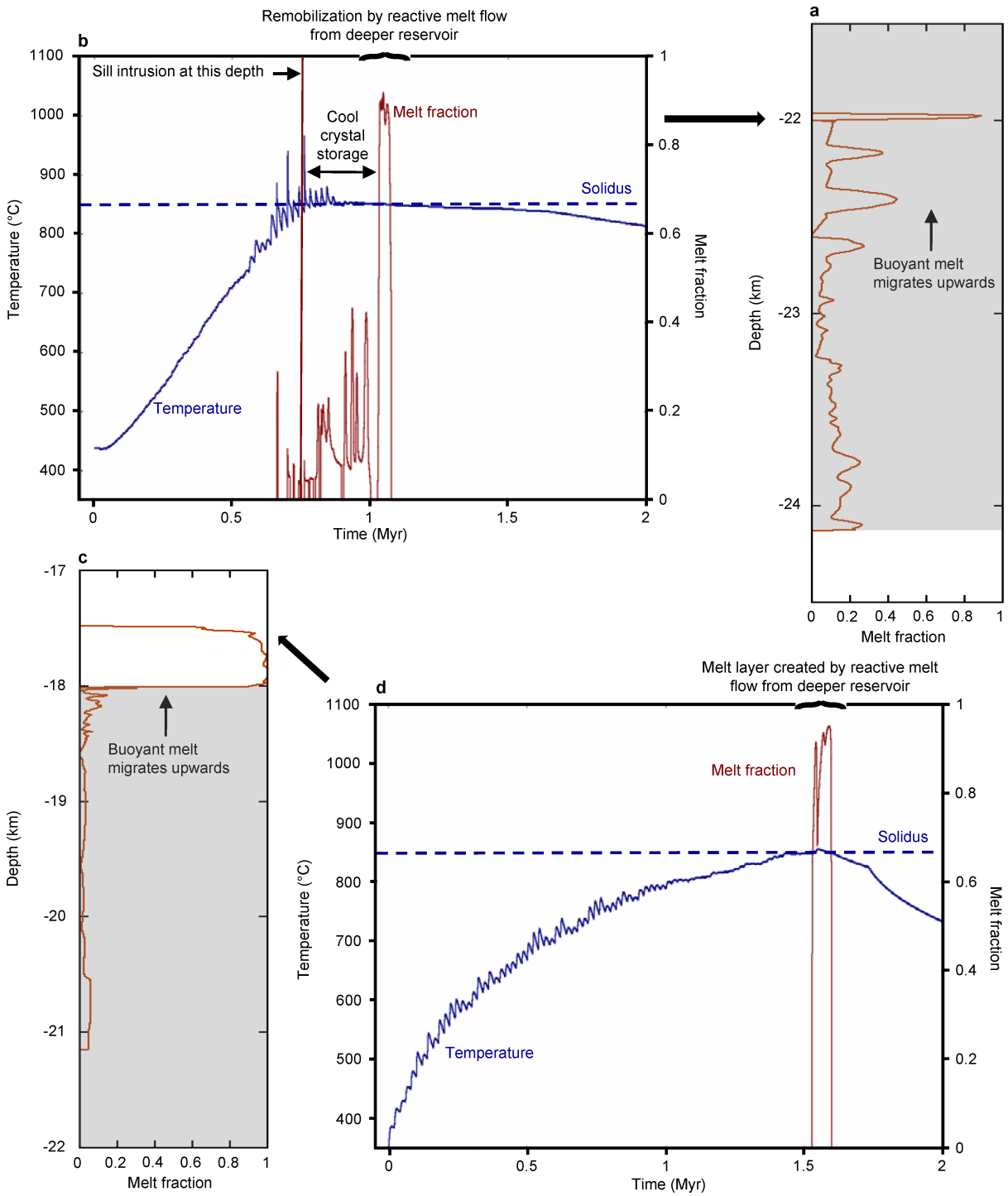

Extended Data Fig. 9 | Consequences of emplacement during under- and over-accretion. a, Melt fraction as a function of depth during under-accretion, at the first snapshot after remobilization at a depth of 22 km (1.02 Myr after the onset of sill intrusions). Reactive flow of evolved, buoyant melt produces a high-melt-fraction layer that migrates upwards. **b**, Temperature and melt fraction as a function of time at a depth of 22 km during under-accretion. Similar results are obtained over the depth range 22–22.5 km. Under-accretion causes the sill intrusion depth to increase progressively from 18 km; in this case, an intrusion at 22 km occurs at 0.75 Myr ago that rapidly cools and crystallizes. The crystals are kept in 'cool storage' at a close-to-solidus temperature. At 1.02 Myr the high-melt-fraction layer arrives at this depth and the reservoir is remobilized. **c**, Melt fraction as a function of depth during over-accretion, at a snapshot in time (1.53 Myr after the onset of sill intrusions). In this case, the high-melt-fraction layer has migrated into the overlying country rock. **d**, Temperature and melt fraction as a function of time at a depth of 17.5 km during over-accretion, close to the top of the active magma reservoir. Similar results are obtained over the depth range 17.5–18 km. Crystals in the magma are sourced from the country rock and may be genetically unrelated to the melt. There is no cold storage of crystals brought into the reservoir by basaltic sill intrusions, as intrusion occurs deeper in the reservoir. In **a** and **c**, the shaded area denotes intruded basalt.

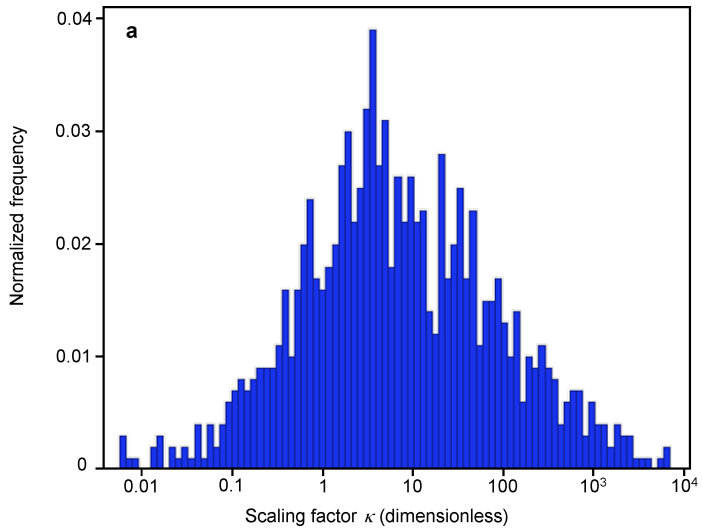

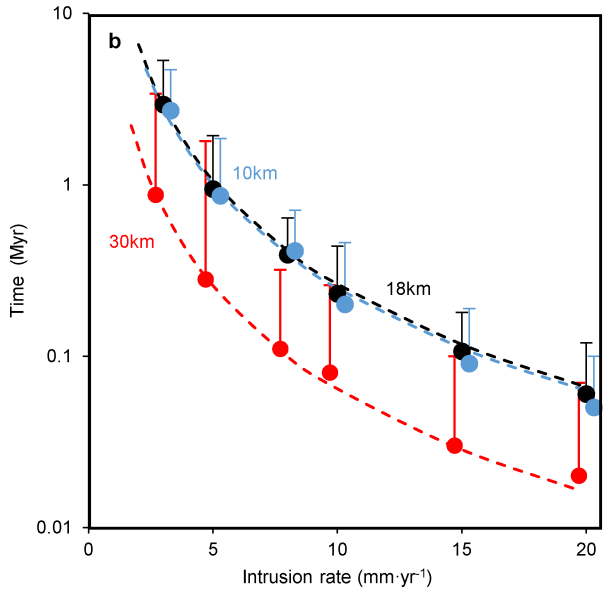

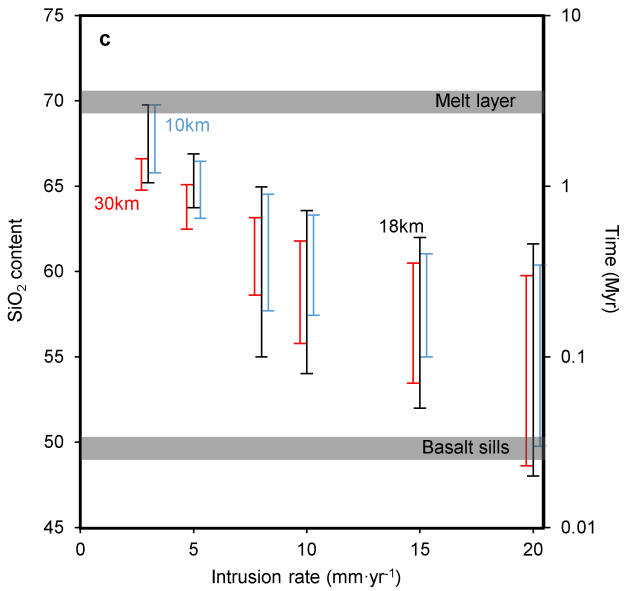

Extended Data Fig. 10 | Sensitivity analysis. a, A frequency plot showing values of the dimensionless scaling factor κ calculated using equation (12). Values of the input values were varied uniformly over the range given in Extended Data Table 1 in a simple Monte Carlo analysis[89]. **b**, Incubation and activation time; **c**, Cold storage time and eruptible magma composition. Error bars and shaded regions in **b** and **c** denote the effect of varying the dimensionless scaling factor κ over the range $0.028 < \kappa < 2{,}160$. Error bars on the incubation time are within the symbol size. Dashed lines denote the fit to the incubation time of the form q^{-2}, where q is the intrusion rate. Colours in **b** and **c** denote different initial emplacement depths of 10 km, 18 km and 30 km. Models were run for a maximum 20 km of intruded basalt.

Extended Data Table 1 | Parameters used in the numerical experiments

Symbol	Description and sources	Example case	Sensitivity analysis	Units
k_T	thermal conductivity[22,23,33,51]	3	1 - 3	$W{\cdot}°C^{-1}{\cdot}m^{-1}$
c_p	specific heat capacity[51]	1100	1,020 - 1,220	$J{\cdot}kg^{-1}{\cdot}°C^{-1}$
L_f	latent heat[51]	550000	400,000 - 600,000	$J{\cdot}kg^{-1}$
T_L-T_S	liquidus-solidus interval[12,73,74]	310	310	°C
T_S	solidus[12,73,74]	850	850	°C
T_{geo}	initial geotherm[21-23,51]	20	20, 40	$°C{\cdot}km^{-1}$
a	matrix grain radius[51]	2.75×10^{-3}	5×10^{-4} - 5×10^{-3}	m
α	permeability exponent[51]	3	3	None
β	bulk viscosity exponent[51]	0.5	0.5	None
b	permeability constant[51]	1/125	1/2500 - 1/50	None
μ_{max}	shear viscosity of most evolved melt[58]	10^5	10^4 – 10^6	Pa·s
μ_{min}	shear viscosity of least evolved melt[58]	1	1	Pa·s
η_r	reference matrix shear viscosity[26,50,51,57]	10^{15}	10^{14} – 10^{17}	Pa·s
q	sill intrusion rate[21-24,32-34]	5	1 - 20	$mm{\cdot}yr^{-1}$
z_s	sill thickness[21-23,42]	100	50-200	m
a_1, a_2, a_3	phase behavior parameters	50, -360, 1433.15	50, -360, 1433.15	°C
a_4, a_5, a_6, a_7, a_8	silica content modelling parameters	62.7, 12.38,-0.0158, 15.44	62.7, 12.38, -0.0158, 15.44	-
ρ_r	reference density[77]	2850	2850	$kg{\cdot}m^{-3}$
ρ_{smin}	density of most evolved solid composition[25,76,77]	3000	3000	$kg{\cdot}m^{-3}$
ρ_{smax}	density of least evolved solid composition[25,76,77]	2600	2600	$kg{\cdot}m^{-3}$
ρ_{mmin}	density of most evolved melt composition[26,76,77]	2880	2880	$kg{\cdot}m^{-3}$
ρ_{mmax}	density of least evolved melt composition[25,76,77]	2350	2350	$kg{\cdot}m^{-3}$
$S^{max}_{SiO_2}$	SiO_2 of most evolved composition[12,73,74]	75	75	%
$S^{min}_{SiO_2}$	SiO_2 of least evolved composition[12,73,74]	50	50	%
K	Trace element Nernst partition coefficient[16]	0.08	0.08	-

Values used to produce the results shown in all figures except Extended Data Fig. 10. A steeper geotherm suitable for thermally mature crust[23] was assumed for the results shown in Extended Data Figs. 4–8, which have intrusion at 10 km depth. The range of values for the sensitivity analysis was used to calculate the range of values of the dimensionless scaling factor κ shown in Extended Data Fig. 10a and to produce the associated numerical modelling results shown in Extended Data Fig. 10b, c. Data sources[12,16,21–26,32–34,42,50,51,57,58,73,74,76,77] are indicated.